AGU PUBLICATIONS

JGR

Journal of Geophysical Research: Atmospheres

RESEARCH ARTICLE
10.1002/2016JD024894

Key Points:
- Submicrometer particles dominate the measured ice residual population by number
- Increase in ice activated fraction with particle size
- Black carbon containing particles are not efficient ice nuclei in mixed-phase clouds

Supporting Information:
- Supporting Information S1

Correspondence to:
M. Gysel,
martin.gysel@psi.ch

Citation:
Kupiszewski, P., et al. (2016), Ice residual properties in mixed-phase clouds at the high-alpine Jungfraujoch site, *J. Geophys. Res. Atmos.*, *121*, 12,343–12,362, doi:10.1002/2016JD024894.

Received 3 FEB 2016
Accepted 20 SEP 2016
Accepted article online 26 SEP 2016
Published online 26 OCT 2016

Ice residual properties in mixed-phase clouds at the high-alpine Jungfraujoch site

Piotr Kupiszewski[1,2], Marco Zanatta[1,3,4], Stephan Mertes[5], Paul Vochezer[6], Gary Lloyd[7], Johannes Schneider[8], Ludwig Schenk[5], Martin Schnaiter[6], Urs Baltensperger[1], Ernest Weingartner[1,9], and Martin Gysel[1]

[1]Laboratory of Atmospheric Chemistry, Paul Scherrer Institute, Villigen, Switzerland, [2]Now at Department of Meteorology, Stockholm University, Stockholm, Sweden, [3]Laboratoire de Glaciologie et Géophysique de l'Environnement, Université Grenoble Alpes/CNRS, Grenoble, France, [4]Now at Alfred Wegener Institute, Helmholtz Centre for Polar and Marine Research, Bremerhaven, Germany, [5]Leibniz Institute for Tropospheric Research, Leipzig, Germany, [6]Institute of Meteorology and Climate Research, Karlsruhe Institute of Technology, Karlsruhe, Germany, [7]Centre for Atmospheric Science, SEAES, University of Manchester, Manchester, UK, [8]Particle Chemistry Department, Max Planck Institute for Chemistry, Mainz, Germany, [9]Now at Institute for Aerosol and Sensor Technology, University of Applied Sciences, Windisch, Switzerland

Abstract Ice residual (IR) and total aerosol properties were measured in mixed-phase clouds (MPCs) at the high-alpine Jungfraujoch research station. Black carbon (BC) content and coating thickness of BC-containing particles were determined using single-particle soot photometers. The ice activated fraction (IAF), derived from a comparison of IR and total aerosol particle size distributions, showed an enrichment of large particles in the IR, with an increase in the IAF from values on the order of 10^{-4} to 10^{-3} for 100 nm (diameter) particles to 0.2 to 0.3 for 1 μm (diameter) particles. Nonetheless, due to the high number fraction of submicrometer particles with respect to total particle number, IR size distributions were still dominated by the submicrometer aerosol. A comparison of simultaneously measured number size distributions of BC-free and BC-containing IR and total aerosol particles showed depletion of BC by number in the IR, suggesting that BC does not play a significant role in ice nucleation in MPCs at the Jungfraujoch. The potential anthropogenic climate impact of BC via the glaciation effect in MPCs is therefore likely to be negligible at this site and in environments with similar meteorological conditions and a similar aerosol population. The IAF of the BC-containing particles also increased with total particle size, in a similar manner as for the BC-free particles, but on a level 1 order of magnitude lower. Furthermore, BC-containing IR were found to have a thicker coating than the BC-containing total aerosol, suggesting the importance of atmospheric aging for ice nucleation.

1. Introduction

At temperatures above −38°C, i.e., above the limit below which homogeneous freezing of liquid droplets occurs in mixed-phase clouds (MPCs), formation of ice in the atmosphere takes place on the surface of aerosol particles referred to as ice nucleating particles (INP) [*Hoose and Möhler*, 2012]. These particles lower the Gibbs-free energy barrier of nucleation and can thus trigger heterogeneous ice nucleation at higher temperatures than would be required for homogeneous nucleation [*Lamb and Verlinde*, 2011]. INP are very few in number compared to the total aerosol. At −10°C the number concentration of INP is as much as 7 to 9 orders of magnitude lower than that of the total aerosol [*Szyrmer and Zawadzki*, 1997], while at −20°C it is approximately 5 orders of magnitude lower [*Pruppacher and Klett*, 1997]. Consequently, in the temperature range 0 to −38°C the presence of INP, in combination with cloud dynamics, largely regulates the phase of the clouds, which can be liquid, glaciated, or mixed phase, i.e., containing both supercooled liquid droplets and ice crystals. Under certain conditions secondary ice production processes also affect cloud glaciation, most notably through splinter production during riming of ice particles in the temperature range of −8 to −3°C (Hallet-Mossop process) [*Hallett and Mossop*, 1974; *Phillips et al.*, 2001; *Saunders and Hosseini*, 2001]. Other mechanisms, such as secondary ice production initiated by freezing of large droplets in strong tropical cumulus updrafts in the temperature range of −15 to −8°C [*Lawson et al.*, 2015] or mechanical breakup of ice particles as a result of ice-ice collisions [*Yano and Phillips*, 2011], have also been suggested.

Formation of ice in the atmosphere affects cloud microphysical properties, which in turn influence radiative transfer and precipitation formation. In mixed-phase clouds, under favorable thermodynamic conditions, rapid growth of ice crystals at the expense of liquid droplets can take place via the Wegener-Bergeron-Findeisen process [*Korolev*, 2007; *Lohmann and Feichter*, 2005; *Schwarzenböck et al.*, 2001; *Verheggen et al.*, 2007]. A cloud containing numerous, small liquid droplets can thus be transformed within minutes to a glaciated cloud with much fewer, but larger, ice crystals [*Murray et al.*, 2012]. This results in a strong decrease in the optical depth and albedo of the cloud [*Sun and Shine*, 1994] and can initiate precipitation [*Chen and Lamb*, 1999]. Indirect evidence for the latter is the rapid depletion of INP at moderate supercoolings, as compared to depletion of total aerosol particles of a similar size, during precipitation [*Stopelli et al.*, 2015]. Ice nucleation is thus of major importance for both the radiative properties of clouds and the hydrological cycle of the Earth.

Currently, the properties of INP are not well known with a paucity of field measurements focused on their characterization. The study of ice nucleation is further complicated by the variety of mechanisms or ice nucleation modes [*Vali et al.*, 2015] through which ice formation can occur. There has been a number of aircraft campaigns focused on sampling of ice crystals in cirrus clouds using the counterflow virtual impactor (CVI) technique [*Cziczo et al.*, 2013; *Prenni et al.*, 2007; *Twohy and Poellot*, 2005]. However, MPC measurements are hindered by the difficulties involved in selectively extracting the relatively few ice crystals from among the much more numerous supercooled liquid droplets of similar aerodynamic size, as well as interstitial aerosol particles contained within MPCs. As ice nucleation in cirrus clouds takes place under different temperature and supersaturation conditions than in MPCs it is not possible to directly apply results from the former to the latter. Therefore, measurements of ice nucleating particles in MPCs are necessary to improve our understanding of the relevant ice nucleating processes. Aircraft-based CVI sampling of cloud particles at temperatures at which heterogeneous ice nucleation takes place has also been conducted in orographic wave clouds [*Pratt et al.*, 2009, 2010a, 2010b] and mixed-phase clouds [*Hiranuma et al.*, 2013]. However, as the CVI does not discriminate between liquid and ice particles, these measurements were limited either to sampling in a glaciated region of the cloud or when sampling in the mixed-phase region of the cloud, resulted in all cloud residues being collected, whereby both INP and cloud condensation nuclei (CCN) are present and cannot be distinguished. Dedicated measurements of INP in MPCs thus require instrumentation which can selectively extract pristine ice crystals from an MPC.

The Ice-CVI [*Mertes et al.*, 2007] is an inlet which overcomes the aforementioned issues and selectively samples small (5–20 μm aerodynamic diameter) ice crystals. As the transition in ice crystal growth mechanism from diffusional growth to riming is predicted to take place for 50 μm ice crystals [*Mertes et al.*, 2007, and references therein], 5–20 μm ice crystals can be assumed to have grown primarily by water vapor diffusion. Scavenging of interstitial aerosol particles by these freshly formed ice crystals is very unlikely (see section S1 of the supporting information for a discussion of the coagulation rates of ice crystals and interstitial particles) [*Seinfeld and Pandis*, 2006]. Consequently, in the absence of secondary ice formation, the particles left after sublimation of these ice crystals, i.e., the ice residuals (IR), can be considered as the original INP. It should be noted that this assumption may partially break down in the case of sampling of ice crystals formed through freezing of droplets; in this case, the ice residual may also contain CCN material. Nonetheless, the mass and diameter of larger IR should be dominated by the original INP. Following extraction and sublimation of the small ice crystals, detailed measurements of the physical and chemical properties of the IR can be conducted, thus providing more information on the characteristics of INPs in MPCs.

A characterization of IR in MPCs using the Ice-CVI during the CLACE-3 (Cloud and Aerosol Characterization Experiment) campaign at the Jungfraujoch showed that the likelihood of a particle acting as an INP increases with particle size [*Mertes et al.*, 2007]. Nonetheless, the IR were predominantly submicrometer particles, due to the sheer number of submicrometer particles as compared to supermicrometer particles. Previous studies at the Jungfraujoch have identified IR as predominantly containing mineral dust and organics [*Cziczo et al.*, 2009; *Kamphus et al.*, 2010]. Some studies have further identified lead as being strongly enriched in IR [*Cziczo et al.*, 2009; *Ebert et al.*, 2011]. The role of black carbon (BC) is contentious, with varying results among different studies, both in the field and in the laboratory [*Hoose and Möhler*, 2012]. Following field measurements at the Jungfraujoch, *Cozic et al.* [2008] and *Mertes et al.* [2007] reported enrichment by mass of BC in IR based on particle soot absorption photometer (PSAP) measurements, while *Ebert et al.* [2011] found enrichment by number of C-O-S particles (i.e., internal mixtures of organics, nitrates, and sulfates, sometimes containing soot inclusions) in IR relative to the interstitial aerosol using scanning electron microscopy and transmission

electron microscopy. In contrast, based on single-particle mass spectrometer measurements [*Kamphus et al.*, 2010] and multiangle absorption photometer measurements [*Chou et al.*, 2011], no proof for BC influence on ice nucleation in MPCs was found.

This paper focuses on measurements of the physical properties and BC content of IR sampled using the Ice-CVI during the joint CLACE 2013 and Ice Nuclei Research Unit (INUIT) campaign. The campaign was conducted at the high-alpine research station Jungfraujoch in the winter of 2013 with the principal goals of investigating the characteristics of INP [*Boose et al.*, 2016; *Kupiszewski et al.*, 2015; *Worringen et al.*, 2015] and cloud microphysical properties [*Lloyd et al.*, 2015; *Vochezer et al.*, 2016]. Based on an analysis of IR size distributions measured downstream of the Ice-CVI, the size of particles predominantly acting as INP in MPCs is determined. Total aerosol and IR size distributions are compared, allowing for calculation of the ice activated fraction (IAF) of particles as a function of size (the IAF is defined as the number concentration ratio of ice residual particles to total particles for a certain subset of particles detected behind the Ice-CVI and total aerosol inlets). The laser-induced incandescence technique is used to measure BC content in the IR and total aerosol on a single particle basis, providing a robust measurement for determining whether BC is enriched in the IR. In combination with size distribution measurements of BC-containing particles in IR and in the total aerosol this allows for determination of whether BC is an atmospherically relevant INP. Finally, the coating thickness of BC-containing particles is measured, shedding light on the effect of the mixing state of BC particles on their ice nucleating ability.

The presented data set includes, to the best of our knowledge, the most extensive measurements of the physical properties of IR in MPCs conducted to date, with a host of state-of-the-art aerosol probes including an Ultra-High Sensitivity Aerosol Spectrometer (UHSAS), scanning mobility particle sizers (SMPS), Grimm optical particle size spectrometers (OPSSs), a waveband integrated bioaerosol sensor (WIBS3), a TSI optical particle sizer (OPS), and single particle soot photometers (SP2) measuring ice residual size distributions in the range of 0.02–5 μm. Furthermore, it is the first time SP2 measurements of BC in IR at the Jungfraujoch are presented. While measurements of BC in IR and INP have been conducted previously using particle soot absorption photometers [*Cozic et al.*, 2008], a multiangle absorption photometer [*Chou et al.*, 2011], and single-particle mass spectrometers [*Kamphus et al.*, 2010], the SP2 data set is unique in providing detailed single-particle information, including core size and coating thickness, unavailable from any of the other aforementioned instruments.

2. Experimental: CLACE 2013 Field Campaign

The joint CLACE 2013-INUIT campaign was carried out in January and February 2013 at the Jungfraujoch site (3580 m above sea level in the Swiss Alps)—a Global Atmosphere Watch (GAW) research station [*Bukowiecki et al.*, 2016]. The Jungfraujoch is predominantly in the free troposphere during winter (over 60% of the time) [*Herrmann et al.*, 2015] and is frequently in cloud (around 40% of the time) [*Baltensperger et al.*, 1998]. Together with the subzero temperatures prevalent in winter, these characteristics ensure that the site is well suited to the objectives of the campaign.

2.1. Aerosol Inlets: Total Inlet and Ice-CVI

A total aerosol inlet, mounted on the roof of the Sphinx laboratory, is operated year round as part of the GAW monitoring program. All particles below 40 μm in diameter for wind speeds up to 20 m s^{-1} are sampled by the inlet. The tubing is insulated, and the inlet heated to 20°C in order to dry the sampled hydrometeors and avoid transmission losses and to prevent rime buildup on the inlet [*Weingartner et al.*, 1999].

The Ice-CVI, characterized in detail based on modeling and tests conducted in laboratory as well as field experiments by *Mertes et al.* [2007], is an inlet system which employs a series of components to remove snow aggregates, supercooled liquid droplets, and interstitial aerosol particles from air directly sampled in ambient MPCs, thus extracting solely small ice crystals with aerodynamic diameters of 5–20 μm. During the CLACE 2013 campaign the Ice-CVI was set up adjacent to the total inlet, with the inlet of the Ice-CVI mounted ~2 m above the ground. The setup of the Ice-CVI is as follows: air is aspirated through an omnidirectional, roofed inlet which limits the collection of hydrometeors larger than 50 μm [*Mertes et al.*, 2007]. A virtual impactor subsequently removes particles above 20 μm, while all interstitial particles and hydrometeors smaller than 20 μm remain in the sample flow. A two-stage pre-impactor removes the liquid droplets, which freeze onto the impaction plates at temperatures below 0°C, while the ice crystals bounce off and stay in the sample flow.

Finally, a counterflow virtual impactor (CVI) mounted within a wind tunnel [*Schwarzenboeck et al.*, 2000] is used to remove particles smaller than 5 μm. Ice crystals larger than 5 μm (and smaller than 20 μm) are the only condensed phase matter remaining in the sample flow. These ice crystals are transmitted through the CVI and are injected into dry, particle-free air, thus ensuring sublimation of the ice crystals and release of the ice residual particles for further characterization. At times when the research station was out of cloud, the Ice-CVI was operated in total aerosol inlet mode, by switching off the CVI counterflow. Those measurements from the UHSAS and TSI OPS probes (see section 2.3 for instrument descriptions) which are referred to as "total inlet" measurements were obtained in this manner and are not simultaneous with the IR measurements.

2.2. Cloud Probes

2.2.1. Particulate Volume Monitor (PVM-100) and Cloud Droplet Probe

Measurements of liquid water content (LWC) were carried out using a Cloud Droplet Probe (CDP, Droplet Measurement Technologies, USA) [*Lance et al.*, 2010] and two Particulate Volume Monitors (PVM-100, Gerber Scientific Inc., USA) [*Gerber*, 1991; *Wendisch et al.*, 2002]. The CDP is a single-particle instrument which provides a size distribution in the 2–50 μm diameter size range based on the intensity of scattered light at 4–12° in the forward direction from particles passing through a 658 nm laser beam [*Lance et al.*, 2010]. LWC can subsequently be calculated from the measured size distributions. In contrast to the CDP, the PVM-100 measures light scattered by a particle ensemble. A 780 nm laser illuminates particles passing between the transmitter and receiver arms of the instrument, which house the laser diode and receiver optics, respectively. The light scattered in the forward direction is collected by the receiver optics and transmitted through two spatial filters. One of the spatial filters converts the scattered light with scattering-angle-dependent weighting factors to an output signal proportional to the volume concentration of the particle ensemble, i.e., LWC in the case of a droplet ensemble. The second spatial filter converts the scattered light with scattering-angle-dependent weighting factors to an output signal proportional to the surface area concentration. "In-cloud" periods during CLACE 2013 were defined using a LWC threshold value of 0.02 g m^{-3} from 5 min averages of the CDP and PVM-100 measurements (see Table 1 for a list of all measured cloud events). It should be noted that the presence of ice will lead to LWC overestimation in both the CDP and PVM-100 measurements. In the CDP measured optical diameter (D_{opt}) size range of 2–50 μm number concentrations of ice crystals are in general very low in MPCs as compared to the liquid droplet concentrations; therefore, the effect of ice presence on LWC inferred by the CDP should be minimal. The effect is likely larger for the PVM-100, as it does not have a size cut, and larger ice particles will thus also contribute to the PVM-100 signal. As we are interested in LWC only as a determinant of cloud presence, overestimation of LWC due to additional light scattering from ice crystals is not considered to be an issue.

2.2.2. Small Ice Detector

The number, size, shape, and phase of hydrometeors were measured using the Small Ice Detector (SID-3) [*Kaye et al.*, 2008; *Ulanowski et al.*, 2014; *Vochezer et al.*, 2016], which acquires light scattering patterns from particles passing through a laser beam with a wavelength of 532 nm. The particles are counted and sized based on the scattered light intensity detected in the range of 40.75–59.25° relative to the forward direction. The shape and phase of cloud particles are deduced from high-resolution scattering patterns which are recorded by an intensified CCD camera in the 8–23° forward direction. The camera exposure trigger threshold can be adjusted. Typically, the trigger threshold was set high enough to avoid acquisition of liquid droplet scattering patterns. However, this also prevents the acquisition of small ice crystal scattering patterns. During several periods only, the trigger threshold was lowered so that measurements of cloud particles in the 2–28 μm size range could be made. During CLACE 2013 the SID-3 was mounted on a rotating platform, which automatically adjusted to shifts in the wind direction. The high-resolution scattering patterns obtained contain detailed information on the phase and habit of individual cloud particles. In order to distinguish the phase of the particles, their azimuthal symmetry is analyzed. This is based on the fact that a spherical droplet generates an airy pattern with perfect azimuthal symmetry, as opposed to ice crystal scattering patterns, which have lower azimuthal symmetry. Further details on the data retrieval procedure and associated uncertainties can be found in *Vochezer et al.* [2016].

2.3. Aerosol Number Concentration, Size Distribution, and Composition Measurements

Aerosol number concentration, size distribution, and composition were measured downstream of the total inlet (TI) and the Ice-CVI by a host of instruments described below. The sampling positions of the instruments are given in Table 2 together with the size ranges measured. All size distributions measured downstream of the Ice-CVI were corrected for the enrichment of particles by the CVI component of the Ice-CVI

Table 1. Average Temperature, Wind Speed, Liquid Water Content, and Ice Mass Fraction During CLACE 2013 Cloud Events

Cloud Event	Cloud Start Time	Cloud End Time	Cloud Duration (HH:MM)	Temperature (°C)	Wind Speed (m/s)	CDP Liquid Water Content (g/m^3)	PVM Liquid Water Content (g/m^3)	Ice Mass fraction
1	27.01.2013 15:30	28.01.2013 10:30	19:00	−12.2	8.2	0.22	-	0.17
2	29.01.2013 01:30	30.01.2013 00:05	22:35	−8.0	12.5	0.29	-	0.13
3	30.01.2013 16:00	31.01.2013 02:00	10:00	−8.4	16.7	0.35	-	0.31
4	31.01.2013 18:30	03.02.2013 11:00	64:30	−15.1	13.3	0.22	0.26	0.29
5	03.02.2013 21:45	04.02.2013 12:30	14:45	−14.4	15.0	0.38	0.51	0.31
6	04.02.2013 16:00	04.02.2013 21:30	5:30	−12.0	10.6	0.29	0.17	0.02
7	05.02.2013 07:30	05.02.2013 09:15	1:45	−14.7	11.9	0.03	0.07	0.09
8	05.02.2013 14:45	06.02.2013 05:25	14:40	−19.4	10.6	0.12	0.05	0.30
9	06.02.2013 08:05	08.02.2013 12:50	52:45	−23.2	8.0	0.30	-	0.18
10	08.02.2013 22:30	09.02.2013 19:00	20:30	−26.6	7.1	0.25	0.19	0.12
11	10.02.2013 16:00	10.02.2013 23:50	7:50	−16.1	9.6	0.07	0.38	0.13
12	11.02.2013 06:20	12.02.2013 06:30	24:10	−18.5	6.6	0.12	0.08	0.07
13	12.02.2013 12:00	13.02.2013 01:20	13:20	−19.4	7.3	0.36	-	0.09
14	14.02.2013 18:30	16.02.2013 02:05	31:35	−16.9	7.7	0.26	0.19	0.12
15	17.02.2013 13:00	17.02.2013 14:00	1:00	−17.1	0.8	-	0.02	0.00
16	17.02.2013 17:30	17.02.2013 19:15	1:45	−20.6	2.2	-	0.04	0.00
17	17.02.2013 21:45	18.02.2013 02:45	5:00	−21.1	8.2	-	0.04	0.01
18	19.02.2013 15:00	20.02.2013 19:05	28:05	−14.3	8.4	-	0.18	-
19	21.02.2013 11:15	21.02.2013 17:30	6:15	−18.8	4.9	-	0.03	-
20	21.02.2013 18:15	21.02.2013 19:30	1:15	−21.3	3.3	-	0.03	-
21	21.02.2013 20:30	21.02.2013 22:15	1:45	−22.3	5.2	-	0.06	-

[*Mertes et al.*, 2007]. For averaging over cloud events and total inlet measurement events, data with time resolutions of 1 min for the optical particle size spectrometers and single particle soot photometers and 6 min for the scanning mobility particle sizers were used, unless stated otherwise. Due to different instrument operating principles, different diameter types are used when presenting the size distributions, namely, mobility diameter, optical diameter, and BC mass equivalent diameter. It should be noted that the different diameter measurements cannot be compared on a one-to-one basis.

Table 2. CLACE 2013 Aerosol Instrumentation Sampling Downstream of the Total Inlet and the Ice-CVI[a]

Instrument	Total Inlet	Ice-CVI	Measured Property	Diameter Range (μm)
CPC model 3010	✓[b]	✓	number concentration	>0.01
UHSAS	✓[b]	✓	size distribution (versus optical diameter)	0.06–1
SMPS @ TI	✓	×	size distribution (versus mobility diameter)	0.016–0.53
SMPS @ Ice-CVI	×	✓	size distribution (versus mobility diameter)	0.016–0.42
Grimm 1 (model 1.129)	✓	✓	size distribution (versus optical diameter)	0.25–32
Grimm 2 (model 1.108)	✓	×	size distribution (versus optical diameter)	0.3–20
TSI OPS model 3330	✓[b]	✓	size distribution (versus optical diameter)	0.3–10
WIBS3	✓	✓	size distribution (versus optical diameter)	0.8–20
SP2[c]	✓	✓	size distribution (versus optical diameter)	0.17–0.44
			BC core mass size distribution (versus BC mass equivalent diameter)	0.08–0.31

[a]Check marks under both "total inlet" and "Ice–CVI" for a given instrument indicate that the instrument was switched between the two inlets.
[b]Measurements of the total aerosol conducted using the Ice–CVI in total inlet mode, as described in section 2.1.
[c]Two SP2 instruments were operated, with one measuring downstream of the total inlet and one measuring downstream of the Ice-CVI.

In order to verify that measured in-cloud ice residual number size distributions are not significantly affected by sampling artifacts (e.g., transmission of interstitial aerosol particles, wind-blown snow, or a memory effect of the long, multicomponent Ice-CVI system), out-of-cloud (background) size distributions were measured downstream of the Ice-CVI. A discussion of the background size distributions (Figure S1) and ratios of in-cloud to out-of-cloud measurements (Figure S2) can be found in section S2 of the supporting information. In brief, a comparison of event-based background size distributions with in-cloud size distributions (the latter are presented in Figure 5), and the resulting ratios of in-cloud to out-of-cloud measurements, shows that background, out-of-cloud particle number size distributions are on the order of 1 magnitude lower than in-cloud ice residual number size distributions. Therefore, while the combination of nonsimultaneous in-cloud and background measurements and the high in-cloud variability in the concentrations of ice residuals introduces considerable uncertainty in the comparison, we conclude that transmission of interstitial aerosol particles generally does not have any meaningful contribution to the ice residual number size distributions. By comparing concentrations of particles measured downstream of the Ice-CVI in liquid and in ice-containing clouds (see section S2 of the supporting information for further discussion and a definition of the threshold used for defining liquid versus ice-containing clouds) we have also verified that the potential breakthrough of droplets does not have any significant effect on the measured ice residual concentrations. The concentrations downstream of the Ice-CVI in liquid clouds are an order of magnitude lower than the concentrations in ice-containing clouds. As this is very similar to the ratio found when comparing background (out-of-cloud) and in-cloud concentrations, the particles measured in liquid clouds can most likely be attributed to the Ice-CVI background, which is also present out of cloud. The finding that there is no additional effect on Ice-CVI concentrations when sampling in liquid clouds as compared to out-of-cloud background concentration measurements is consistent with *Mertes et al.* [2007].

2.3.1. Scanning Mobility Particle Sizers

For the size-resolved measurement of aerosol particles two scanning mobility particle sizers (SMPS) were deployed, one downstream of the total inlet (denoted further on as SMPS TI) and one downstream of the Ice-CVI (denoted further on as SMPS Ice-CVI). SMPS TI covered the mobility diameter (D_{mob}) range from 16 to 530 nm, while the SMPS Ice-CVI covered a smaller mobility diameter range from 16 to 420 nm. For further details on the setup of the SMPS systems and corrections applied to the SMPS measurements, the reader is referred to section S3 of the supporting information [*von der Weiden et al.*, 2009; *Wiedensohler et al.*, 2012].

2.3.2. Optical Particle Size Spectrometers (UHSAS, Grimm OPSS, WIBS3, and TSI OPS)

The Ultra-High Sensitivity Aerosol Spectrometer (UHSAS) [*Cai et al.*, 2008], the Grimm 1.108 and Grimm 1.129 [*Burkart et al.*, 2010], and the TSI optical particle sizer (OPS) model 3330 all belong to the optical particle size spectrometer (OPSS) family of instruments, and operate on the same principle, whereby the intensity of light scattered by particles passing through a laser beam is measured and converted into an optical diameter. The WIBS3 [*Foot et al.*, 2008; *Gabey et al.*, 2010; *Kaye et al.*, 2005] additionally measures ultraviolet light-induced fluorescence; however, particle sizing in the instrument is conducted using the same method as standard OPSS instruments. As particle fluorescence measurements are not within the scope of this paper and only the particle sizing data are used, the WIBS3 is described alongside the other OPSS instruments.

The Grimm 1.129 (denoted as Grimm 1), Grimm 1.108 (denoted as Grimm 2), WIBS3, and TSI OPS measure aerosol particles in the diameter size ranges of 0.25–32 μm, 0.3–20 μm, 0.8–20 μm, and 0.3–10 μm, respectively, while the UHSAS employs a high-intensity intracavity laser to detect and size particles between 60 and 1000 nm optical diameter. Although size distributions are measured up to 32 μm, all size distributions are shown for sizes up to 5 μm due to the cutoff of the CVI component of the Ice-CVI; interstitial particles above this size can be transmitted through the CVI and cannot be distinguished from true ice residuals, thus leading to potential contamination of the signal. Further information on the setup and calibration of the OPSS instruments, the data corrections applied and the measurement errors are provided in section S4 of the supporting information [*Kaye et al.*, 2005; *Foot et al.*, 2008; *Gabey et al.*, 2010, 2011].

2.3.3. Single Particle Soot Photometers

Number concentration, size distribution, and mixing state of refractory black carbon (rBC) were monitored using single particle soot photometers (SP2) manufactured by Droplet Measurement Technologies (Boulder, CO, USA). Two four-channel SP2s were deployed during the campaign; one sampled the total aerosol, while the second measured the IR downstream of the Ice-CVI inlet. A comprehensive description of the SP2 operation principles is given by *Stephens et al.* [2003], *Schwarz et al.* [2006], and *Moteki and Kondo* [2007]. In brief, absorbing refractory particles passing through a 1064 nm high-fluence Nd:YAG laser beam are brought to

their boiling point. The peak of the thermal radiation emitted by the incandescent BC core of a single particle is proportional to the mass of rBC contained in the particle. This dependency was calibrated during multiple calibrations using size-selected fullerene soot (Alpha Aesar; #FS12S011) according to *Baumgardner et al.* [2012], *Gysel et al.* [2011], *Laborde et al.* [2012a], and *Moteki et al.* [2010]. Measured rBC mass of a single particle is converted to a rBC mass equivalent diameter (D_{MEV}) using a void-free BC material density of 1800 kg m^{-3} [*Moteki et al.*, 2010]. Detection of light scattered into a solid angle subtended from 13° to 77° and from 103° to 167° with respect to the laser beam axis [*Gao et al.*, 2007] enables optical sizing of the sampled aerosol. The peak of the scattering signal is converted into the partial scattering cross section using a calibration coefficient defined during in situ calibrations carried out with spherical polystyrene latex size standards (Thermo Scientific, formerly Duke Scientific). The optical size is then calculated from the calibrated partial scattering cross section using Mie theory and assuming that the particles are spherical. A refractive index of 1.59 was used for the calibration, while 1.50 was assumed for measurements of the total aerosol and IR. The SP2 design ensures 100% detection efficiency for particles above the lower size limit of detection, which corresponds to a $D_{MEV} = 80$ nm for rBC cores. As the SP2 is a quantitative, single-particle instrument, there is no number or mass concentration lower limit of detection, making it well suited to IR measurements. The leading edge only (LEO) method introduced by *Gao et al.* [2007] and slightly adapted by *Laborde et al.* [2012b] was applied for the optical sizing of all particles in order to avoid interference from particle evaporation within the laser beam for BC-containing particles. The partial scattering cross section derived from the LEO fit was converted to an optical diameter using Mie theory and assuming a homogeneous sphere or a concentric spheres core-shell structure for BC-free and BC-containing particles, respectively. The rBC core, if present, is assumed to have an index of refraction of $2.26 + 1.26i$ [*Moteki et al.*, 2010], while the coating index of refraction is assumed to be 1.50, for consistency with the standard optical sizing. This, together with the BC core size constrained by the incandescence measurement, fully constrains the total particle size. The LEO-fit optical sizing is cross checked against the standard optical sizing and works in the diameter range from 170 to 440 nm. The coating thickness is defined as the difference between the radius of the total particle and the rBC core mass equivalent radius. In this work the coating thickness is only reported for BC cores having a D_{MEV} between 170 and 220 nm. Larger core sizes were not included in the results due to insufficient counting statistics. Agreement of the two SP2s between each other for all measured parameters was verified during the campaign based on simultaneous measurements at the total inlet.

3. Results and Discussion

3.1. Ice-CVI Performance: Comparison of Ice Residual and Small Ice Crystal Number Concentrations

An important step in verifying the operation of the Ice-CVI is a comparison of the IR and small ice crystal number concentrations, e.g., measured with the SID-3. The period 22:00 LT (local time) 8 February 2013 to 07:00 LT 9 February 2013 presented an opportunity for such a comparison between the Ice-CVI and the SID-3. During this period the SID-3 was operated such that it detected small cloud particles in a size range of 2–28 μm, covering the size range of ice crystals extracted by the Ice-CVI (see section 2.2.2 for details on the SID-3 settings). Concurrently, IR number concentrations were recorded by the CPC operated downstream of the Ice-CVI. Figure 1 shows an overview of the air temperature and wind speed measured by MeteoSwiss (Figure 1a), cloud particle size distributions (Figure 1b), the size-resolved ice number fraction (Figure 1c), and small ice crystal ($5\ \mu m < D_{opt} < 20\ \mu m$) and droplet integrated number concentrations (Figure 1d) during the case study period. Air temperature was stable over the period, with values between −26.5 and −25.5°C, while wind speed was 5–7 m s^{-1} over the first half of the period, increasing to approximately 8–10 m s^{-1} during the second half. As seen in Figures 1b and 1d, shortly after 23:00 LT a cloud was formed at the Jungfraujoch and the station remained in-cloud throughout the night. The advected clouds, initially containing only droplets, glaciated over the course of the night with increasingly high ice number fractions (Figure 1c). The increase in ice number fraction is visible particularly at optical diameters above 10–15 μm, where ice becomes dominant in the number fraction; at smaller sizes droplet number fractions remain substantial, although decreasing during the presented period. The time series of small ice crystal (5–20 μm optical diameter) and IR number concentrations (Figure 2) shows that initially more IR than small ice crystals are detected (see section S5 of the supporting information for further details on the intercomparison), but in general the two measurements tracked each other quite well, with the strong increase in number concentrations after 03:00 LT clearly visible in both instruments and a correlation coefficient r^2 of 0.6. It should be noted that during the brief cloud-free period (approximately 22:20–23:00 LT 8 February 2013) the CPC number concentration is close to zero, confirming the very low out-of-cloud background downstream of the Ice-CVI. Note that small ice crystal number

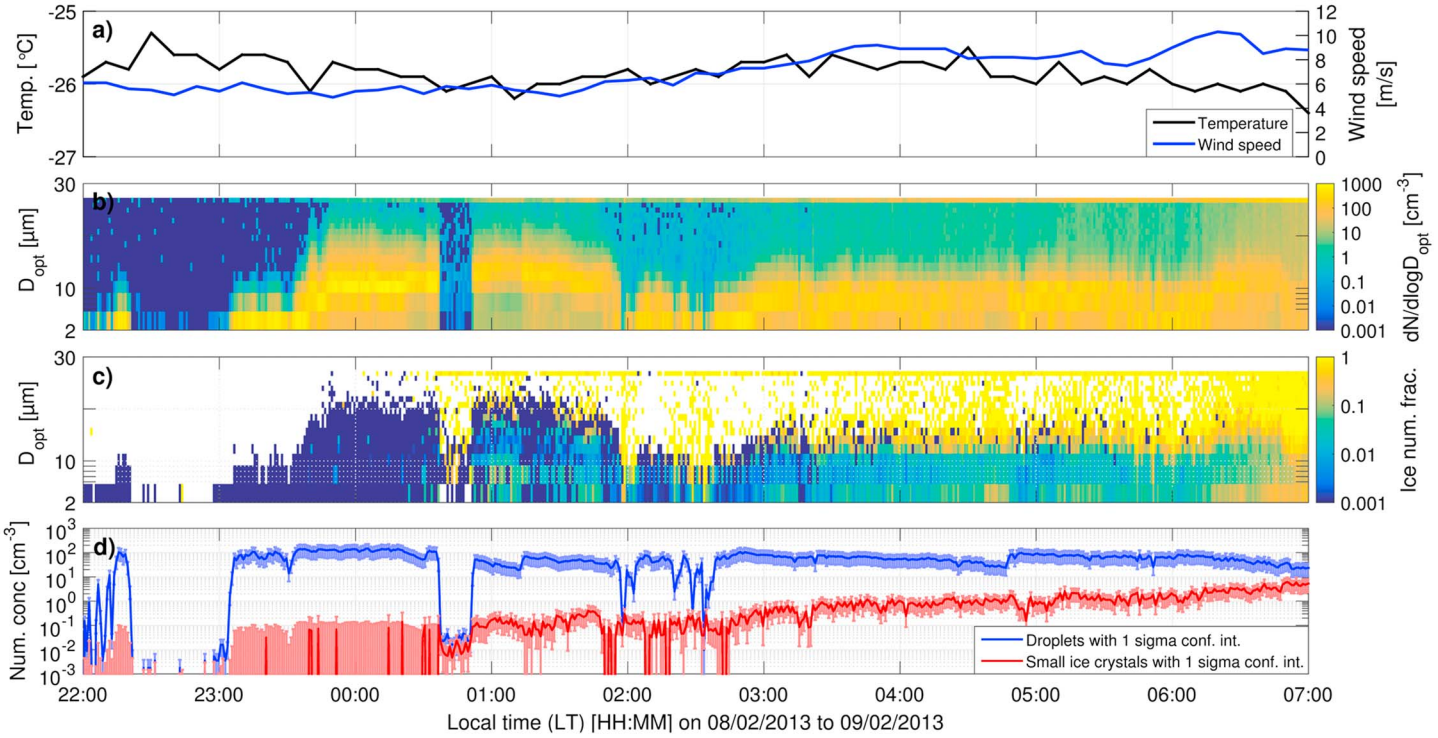

Figure 1. Measurements of air temperature, wind speed, and cloud particles during CLACE 2013, 22:00 LT, 8 February 2013 to 07:00 LT, 9 February 2013. (a) The air temperature and wind speed measured by MeteoSwiss. (b) The size distribution of all cloud particles (droplets and ice particles). (c) The size-resolved ice number fraction. (d) The integrated number concentrations of droplets and small ice crystals in the D_{opt} size range of 5-20 μm obtained from SID-3 measurements.

concentrations in the 2–20 µm and 2–28 µm optical diameter size ranges are also shown in Figure 2 to highlight the strong dependence of the SID-3 number concentration on the optical size range selected (SID-3 optical sizing, which is based on calibrations using spherical liquid droplets, faces considerable uncertainties when sizing ice crystals). Further discussion concerning the level of agreement that can be expected between measurements of IR and small ice crystal number concentrations can be found in section S5 of the supporting information [*Järvinen et al.*, 2016; *Schnaiter et al.*, 2016].

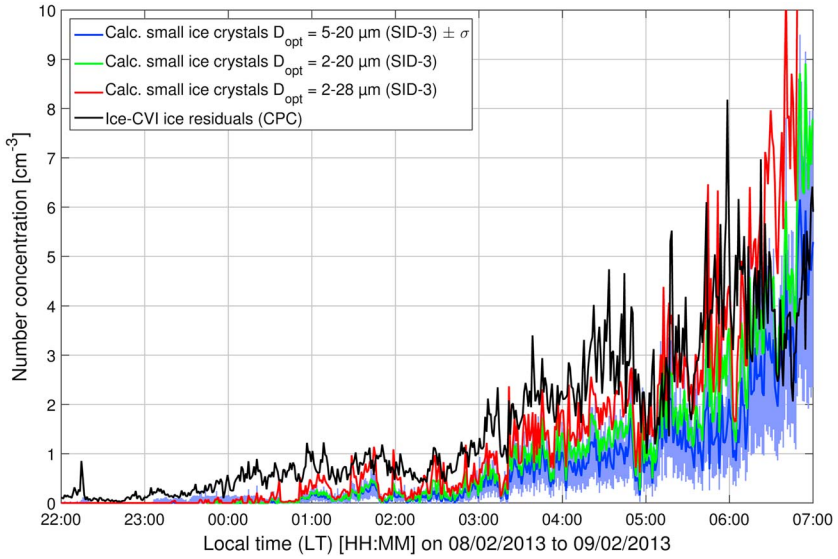

Figure 2. Time series of small ice crystals (D_{opt} size ranges of 5–20 µm, 2–20 µm, and 2–28 µm) number concentrations measured by the SID-3 and ice residual number concentrations measured by the Ice-CVI CPC during CLACE 2013, 22:00 LT, 8 February 2013 to 07:00 LT, 9 February 2013.

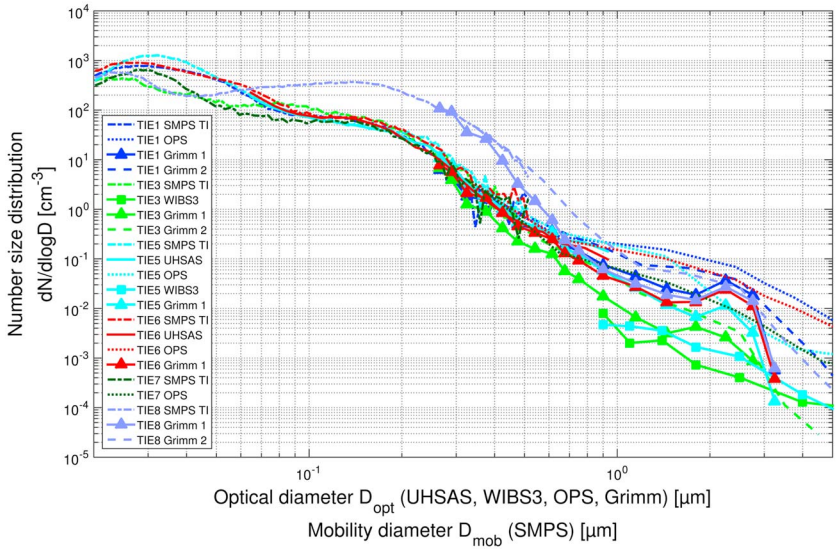

Figure 3. Averages of total aerosol number size distributions during multiple CLACE 2013 total inlet measurement periods. Simultaneous measurements by different instruments during the same event are denoted by a common trace color.

3.2. Assessment of Aerosol Instrument Intercomparability

In order to establish how well the aerosol instruments compare with one another and the magnitude of uncertainties in the size distributions, we compare averaged size distributions of the total aerosol and of IR from the different instruments based on simultaneous measurements. Figure 3 shows six such periods for the total aerosol measurements (total inlet events; TIE), and Figure 4 shows five such periods for the Ice-CVI (cloud events; CE); the size distributions from a given measurement period are denoted by a common color. As shown by the simultaneous measurements, there is very good agreement between instruments for sizes up to a few hundred nanometers. However, at larger sizes the measured size distributions from the optical particle size spectrometers (UHSAS, WIBS3, Grimm OPSSs, and TSI OPS) frequently differ considerably, sometimes by as much as 1 order of magnitude, as is the case, for example, for TIE 5 (cyan traces in Figure 3) and Ice-CVI CE 1b (red traces in Figure 4). While the sizing uncertainties for larger particles are considerable, the resulting differences are not critical for two reasons: First, the majority of IR are found in the

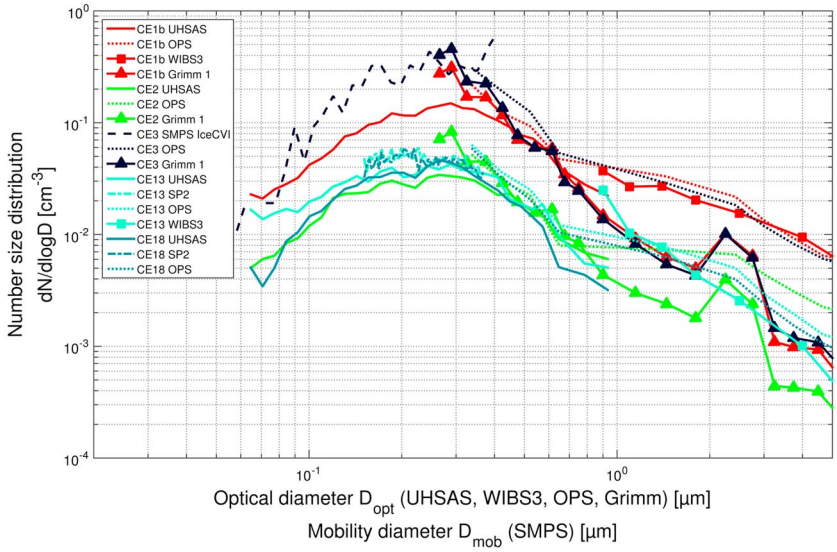

Figure 4. Averages of ice residual number size distributions during multiple CLACE 2013 cloud events. Simultaneous measurements by different instruments during the same cloud event are denoted by a common trace color.

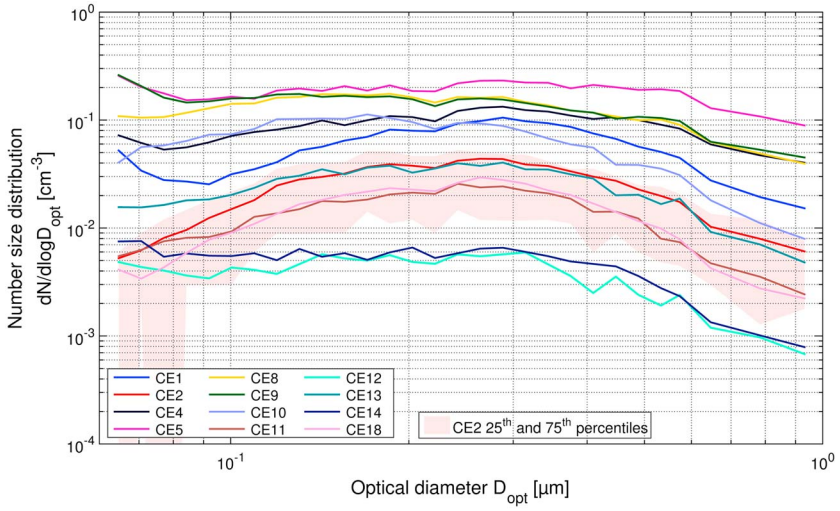

Figure 5. Cloud event averaged ice residual number size distributions measured by the UHSAS (10 min time resolution) during CLACE 2013. Interquartile variability of 10 min averages during a single cloud event is shown for CE2 as an example.

submicrometer size range and thus are affected by these uncertainties to a much smaller degree. Second, the calculated ice activated fractions are based on size distribution ratios between comparable instruments. As a result, the ice activated fractions are not affected by uncertainties, except for the exact particle size corresponding to the inferred IAF values. This size uncertainty is not critical as the IAF depends only moderately on size in the supermicrometer diameter range, as will be shown later. Further discussion of the differences in measured size distributions, the corrections applied, and possible reasons for the inconsistencies between instruments is provided in section S6 of the supporting information.

3.3. Ice Residual Size Distributions

A total of 15 cloud events could be used for the analysis of IR size distributions during CLACE 2013 (Table S1 in section S7 of the supporting information shows a list of instrumentation measuring ice residuals during each cloud event). The variability in size distributions between cloud events can be seen in Figure 5, which shows the mean size distributions measured by the UHSAS for those 12 events during which it was in operation. The size distributions are very similar in shape from cloud to cloud but differ greatly in number concentration, spanning 2 orders of magnitude. The 25th and 75th percentiles of the 10 min measurements for a given CE, plotted here for CE2, show that also variability in the number concentrations of small ice crystals during a single cloud event is considerable, which is qualitatively consistent with high-temporal variability of the observed ice mass fraction (inferred from measurements of liquid water content and ice water content).

A compilation of campaign averages and medians of the size distributions measured by seven aerosol size spectrometers downstream of the total inlet and the Ice-CVI is shown in Figure 6. The total aerosol size distributions show high number concentrations of aerosols below ~0.15 µm, subsequently decreasing sharply with increasing size, which is in agreement with previous literature [*Herrmann et al.*, 2015]. Number concentrations at a size D_{opt} = 1 µm are approximately 3–4 orders of magnitude lower than at D_{opt} = 0.1 µm (see the UHSAS size distribution which spans the optical diameter size range of 0.06–1 µm). Meanwhile, the IR size distributions are much flatter with a mode peaking at ~0.3 µm and decreasing only gradually with increasing particle size. As opposed to the total aerosol measurements, the UHSAS size distributions at D_{opt} = 0.1 µm and D_{opt} = 1 µm show number concentrations on the same order of magnitude. In order to quantify the contribution of particles in a given size range to the IR population, as compared to the total aerosol population, we calculate the number fractions of particles in the size ranges of 0.1–0.5 µm, 0.5–1 µm, and 1–5 µm relative to the total number in the 0.1–5 µm size range. We also calculate the absolute number concentrations in the different size ranges. The combined UHSAS median size distribution between 0.1 and 0.6 µm and the OPS median size distribution above 0.6 µm are used to calculate the integrated number concentrations for the given size ranges. For the total aerosol the respective number fractions are 0.991, 0.006, and 0.003 (absolute number concentrations: 12,472 L^{-1}, 69.8 L^{-1}, and 41.6 L^{-1}), while for the IR there is a clear shift to larger sizes with number fractions of 0.76, 0.13, and 0.11 (absolute number concentrations: 34.4 L^{-1}, 5.7 L^{-1}, and 5.2 L^{-1}),

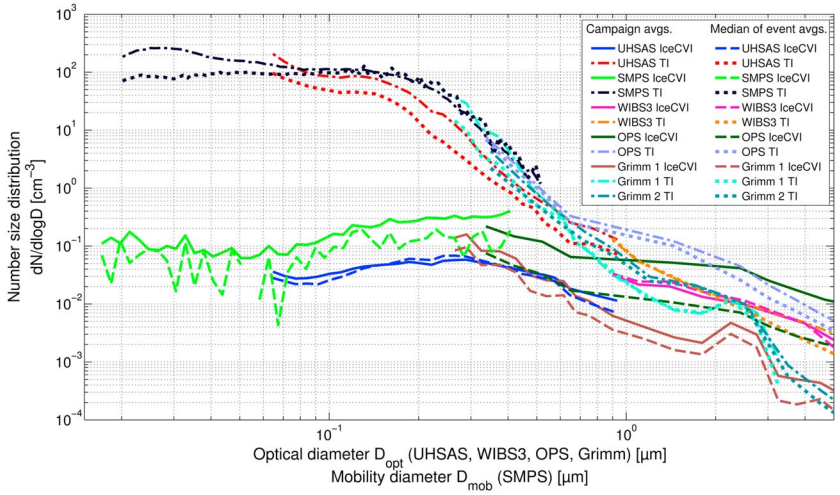

Figure 6. Average and median number size distributions of ice residuals and total aerosol measured during CLACE 2013.

respectively. It should be noted that some instruments were measured exclusively from either the total inlet or the Ice-CVI, while others were switched between the two inlets (see Table 2 for details). This means that the data coverage of each instrument is different. The nonsimultaneous sampling times thus introduce additional uncertainty in the comparison of size distributions from different instruments. The nonsimultaneous sampling periods are, to a large extent, the reason for the difference in the SMPS and UHSAS IR size distributions; a comparison of simultaneous measurements, such as those shown in Figure 4, gives considerably better agreement.

3.3.1. Ice Activated Fraction

The campaign average size distributions presented in Figure 6 were used to calculate the ice activated fraction (IAF) as a function of particle diameter, where the particle diameter is either the mobility diameter (SMPS data) or the optical diameter (UHSAS, Grimm OPSS, WIBS3, and TSI OPS data), shown in Figure 7 for each instrument separately. As discussed in section 3.3, these size distributions are based on nonsimultaneous or only partially simultaneous measurements. The differences between the IAF inferred from different instruments for the same cloud event are thus affected by the variable sampling periods. Nonetheless, the IAF traces show a consistent trend, with the IAF increasing from approximately 10^{-4} to 10^{-3} for 100 nm (diameter)

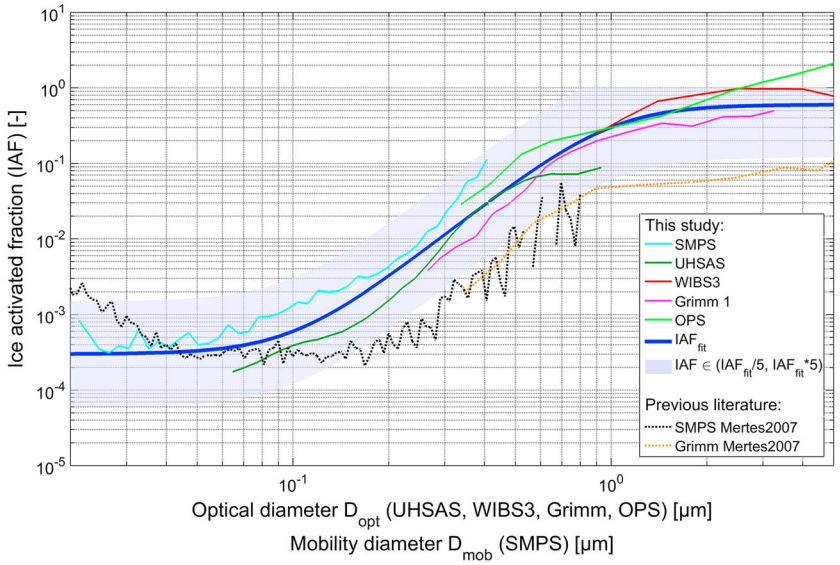

Figure 7. Ice activated fractions (IAF) as a function of optical diameter (D_{opt}) and mobility diameter (D_{mob}) and overall IAF fit during CLACE 2013.

particles to values around 0.2 to 0.3 for 1 μm (diameter) particles. We hypothesize that this increase can be explained by a combination of two effects: First, by an increase in the number of active surface sites [*Connolly et al.*, 2009; *Niedermeier et al.*, 2011] with size for particles with similar composition. The relevance of this effect is supported by the study of *Archuleta et al.* [2005] who found that ice nucleation onset took place at lower relative humidities for larger particles based on continuous flow diffusion chamber measurements of mineral dust surrogates, as well as by *Hung et al.* [2003] who found that larger hematite cores immersed in aqueous ammonium sulfate droplets induced freezing at lower ice supersaturations than smaller hematite cores. Second, the increase in IAF with size could be due to an increase in the number fraction of particles which are good INP, most notably mineral dust, in the total aerosol as a function of size. This is equivalent to an increase in the density of the particles' active surface sites as a function of particle diameter with respect to the total aerosol population. The IAF trend observed in this study is similar to the results reported by *Mertes et al.* [2007] during previous Ice-CVI measurements at the Jungfraujoch (see black and orange dotted traces in Figure 7), although the absolute IAF values are generally several factors higher in this study. However, it should be noted that the results from *Mertes et al.* [2007] are based on a single cloud event of 10 h duration, as compared to several weeks of data presented in this paper, and thus, differences in the absolute values should not be overinterpreted.

In order to provide a means for predicting the number of small (5–20 μm) ice crystals formed, assuming the ambient aerosol size distribution is known, an empirical function has been fit through the measurement-derived IAF traces:

$$\mathrm{IAF}_{\mathrm{fit}}(D_p) = 3.0 \cdot 10^{-4} + \frac{0.6}{1 + D_p^{-3.3}}, \tag{1}$$

where D_p is the particle diameter in micrometers.

The fit is shown in Figure 7 as the blue trace. The blue shading spans the range of $\mathrm{IAF}_{\mathrm{fit}}/5$ and $\mathrm{IAF}_{\mathrm{fit}} \cdot 5$ ($\mathrm{IAF}_{\mathrm{fit}} \cdot 5$ was coerced to 1 at diameters >0.8 μm, where it exceeded the maximum possible IAF of unity). The INP number size distribution can be estimated through multiplication of the ambient aerosol number size distribution ($dN/d\log D$) with the size-dependent IAF as parametrized in equation (1). The total number of INP can subsequently be obtained by integrating the INP number size distribution. It is important to note that this fit is applicable only for conditions and aerosols similar to those experienced during the measurement periods included in this study (a median cloud temperature $T_{\mathrm{med}} = -18.1°\mathrm{C}$ with a first quartile of $T_{\mathrm{Q1}} = -21.3°\mathrm{C}$ and a third quartile of $T_{\mathrm{Q3}} = -13.1°\mathrm{C}$).

In order to put the $\mathrm{IAF}_{\mathrm{fit}}$ into the context of previous work, we calculate the predicted number concentration of INP estimated from the total aerosol size distribution by means of equation (1) and compare this with the INP number concentration predicted based on the parametrization put forward by *DeMott et al.* [2010], henceforth referred to as D2010. For the total aerosol size distribution, required for both approaches, the combined UHSAS median size distribution between 0.1 and 0.6 μm and the OPS median size distribution above 0.6 μm are used. As INP are generally considered to be larger than 0.1 μm [*Marcolli et al.*, 2007; *Pruppacher and Klett*, 1997], we do not consider particles smaller than 0.1 μm to be true INP and do not include such particles in the parametrization. Furthermore, as discussed by *Mertes et al.* [2007], it is possible that small apparent IR sampled downstream of the Ice-CVI originate from small secondary ice particles. *Mertes et al.* [2007] showed that the main increase in the activated fraction started at 0.28 μm and argued that particles above this size do not originate from secondary ice and are representative of the original INP. In order to ensure that we limit any potential sampling artifacts from our analysis and to be consistent with the approach taken by *DeMott et al.* [2010], as the lower size limit, we take 0.5 μm. The resulting number concentration of INP estimated with the parametrization developed in this study is 29 L^{-1}, with the submicrometer fraction (0.5–1 μm) contributing 10 L^{-1} and the supermicrometer fraction (1–5 μm) contributing 19 L^{-1}. It should be noted that these IR number concentrations, which are obtained by applying the parametrization to the total aerosol size distribution, differ considerably from those directly obtained from the measured IR size distribution (see section 3.3). The reason for this discrepancy is differences in the IAF measured by different instruments, which results in high uncertainty of the parametrization. Specifically, the parametrization is a fit through measurements from six different instruments (two SMPS systems, UHSAS, WIBS3, Grimm 1, and OPS), while the IR number concentrations presented in section 3.3 are based only on the median IR size distribution measured by UHSAS and OPS.

Meanwhile, using D2010 with the median cloud temperature T_{med} and the number concentration of total aerosol larger than 0.5 μm $N_{>0.5}$, we obtain INP number concentrations of 0.32 L^{-1}, while INP number concentrations of 0.46 L^{-1} and 0.15 L^{-1} are obtained when using T_{Q1} and T_{Q3}, respectively. The INP number concentrations predicted using equation (1) are thus approximately 2 orders of magnitude higher than the INP number concentrations calculated using D2010. In order to obtain a similar INP concentration as predicted using D2010, we need to take a lower size limit of 3.92 μm in our parametrization; this is an unrealistically high value, highlighting the discrepancies between INP measurements using ice nuclei counters and sampling of IR from ambient clouds.

The reason for the large difference in the INP number concentrations predicted by D2010 and the INP number concentrations predicted in this work is not clear. Some interference from small secondary ice collected by the Ice-CVI cannot be excluded. However, as shown in this work, as well as in previous studies [e.g., *Kamphus et al.*, 2010; *Mertes et al.*, 2007], the IR extracted from small ice crystals have physical and chemical properties different to those of the total aerosol, often with enrichment of particle types which, based on theory and laboratory experiments, would be expected to preferentially act as INP (e.g., larger particles and mineral dust). Sampling of secondary ice which has scavenged ambient aerosol particles would result in similar IR and total aerosol size distributions, and thus a lack of size dependency in the IAF, as well as similar chemical compositions of IR and total aerosol particles, in contrast to what we have observed. The difference in the physical and chemical characteristics of IR and the total aerosol, as well as the limited contribution of secondary ice production to the measured ice crystal concentrations, suggests that the ice crystals sampled are of primary ice origin and the IR extracted acted as INP. Consequently, the D2010 parametrization may provide estimates of INP which are substantially too low for the aerosols and cloud conditions probed at the Jungfraujoch during CLACE 2013. INP number concentrations measured at the Jungfraujoch with an ice nuclei counter by *Chou et al.* [2011] were 1 order of magnitude higher (i.e., a few particles per liter) than predicted using D2010, even though *Chou et al.* [2011] only investigated deposition nucleation, while the data used to derive the D2010 parametrization were taken at water supersaturated conditions and thus included not only deposition nucleation but also condensation and immersion freezing. The order of magnitude higher INP number concentrations measured by *Chou et al.* [2011] as compared to D2010 suggest that the discrepancy in concentrations obtained using our parametrization and using D2010 is not only a result of comparing different methods but also that D2010 is not applicable to the Jungfraujoch. Nonetheless, it is clear that further work is needed to close the gap between measurements of ice crystals, IR, and INP in MPCs.

3.3.2. BC Activation Into Ice

The IAF was also calculated for the subset of measurements obtained using the SP2 instruments. In this case, the IAF is calculated based on periods with simultaneous measurements of the total and Ice-CVI SP2s only. As this is a considerably smaller subset than all data included in Figure 7, the results are shown in a separate figure (IAF as a function of optical diameter is shown in Figure 8). In order to verify the SP2-based results, the measurements were compared with the IAF derived from the SMPS for the same period and showed good agreement (the IAF of the sum of BC-free and BC-containing particles measured by the SP2 and the IAF from the SMPS is given by the blue and red traces, respectively, in Figure 8). The IAF obtained from the SP2 instruments was calculated separately for BC-free particles (green trace in Figure 8) and for incandescing BC-containing particles (black trace in Figure 8). While both traces show an increase in the IAF with increasing particle size, the IAF for BC-containing particles is an order of magnitude lower than the IAF for BC-free particles, for a given total particle size.

The IAF was also calculated for BC-containing particles as a function of the rBC mass equivalent diameter (D_{MEV}) of the BC cores (size distributions of the BC cores in the total aerosol and in the IR are shown in Figure 9 (top), with the resulting IAF displayed in Figure 9 (bottom)). An increase in the IAF from $2 \cdot 10^{-5}$ for BC cores with $D_{MEV} = 0.08$ μm to $5 \cdot 10^{-4}$ for BC cores with $D_{MEV} = 0.29$ μm is observed. The BC mass size distribution observed at Jungfraujoch peaked at 111 nm (geometric mean), which is similar to previous atmospheric observations [*Dahlkötter et al.*, 2014; *Laborde et al.*, 2013; *Moteki et al.*, 2012; *Schwarz et al.*, 2008]. The total aerosol BC number size distribution peaks below a BC core diameter of 100 nm and decreases with size, reaching a value 1 order of magnitude lower for a core size $D_{MEV} = 200$ nm and 2 orders of magnitude lower for a core size $D_{MEV} = 290$ nm. The IR BC number size distribution also peaks below a BC core diameter of 100 nm; however, it decreases much more gradually and is approximately a factor of 2 lower for a core size $D_{MEV} = 200$ nm and a factor of 4 lower for a core size $D_{MEV} = 290$ nm. The number-weighted mean activation ratio of BC-containing particles is below 10^{-4}, i.e., much lower than that of all particles, implying that,

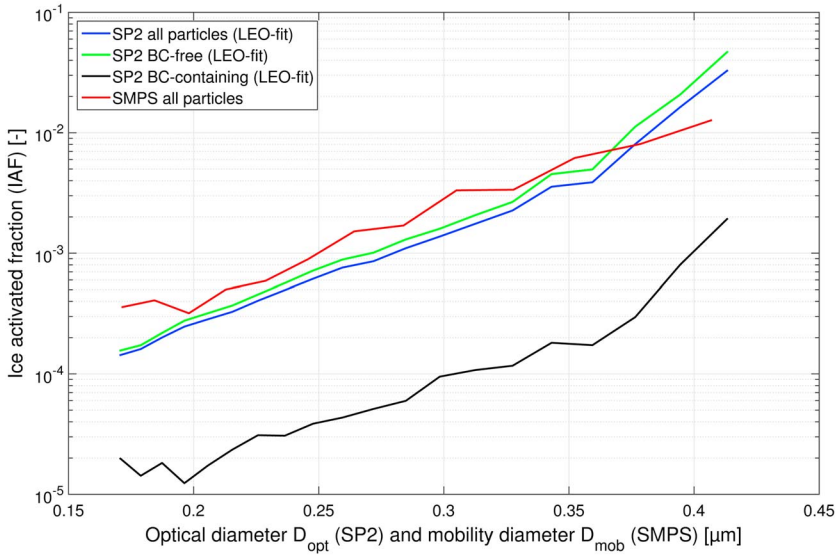

Figure 8. Ice activated fractions (IAF) for BC-free particles, BC-containing particles, and all particles as a function of optical diameter (D_{opt}) as inferred from the SP2 data. The IAF of all particles as a function of mobility diameter (D_{mob}) as measured by the SMPS during the same periods is shown for comparison. Note that the SP2 measurements shown here only covered a subset of the cloud periods included in Figure 7. This subset turned out to have below-average IAF for all particles, which explains the difference between the SMPS results shown here as compared to those shown in Figure 7.

on average, BC-containing particles are very poor INP in the probed MPC conditions. Note that some unusual incandescence signals were detected by the SP2, characterized by slower signal rise and decay times as well as different color ratios when compared to incandescence signals from normal BC-containing particles. All unusual incandescence signals, which are most likely a non-BC interference from, e.g., dust or other metal-containing particles, were associated with supermicrometer-sized particles. Therefore, this interference does not at all affect the results presented in Figure 8, which is restricted to particles in the size range below ~420 nm in diameter. All unusual incandescence signals were filtered for the analysis presented in Figure 9, in which the abscissa is based on the incandescence signal amplitude. Keeping them would have no effect on the total BC core size distribution (blue line in Figure 9 (top)), whereas the BC core size distribution of the ice residual particles (green line in Figure 9 (top)) and the IAF (Figure 9 (bottom)) would increase by less than a factor of 2, thus not changing the basic finding that the IAF at a certain BC core size is on the order of 10^{-4}.

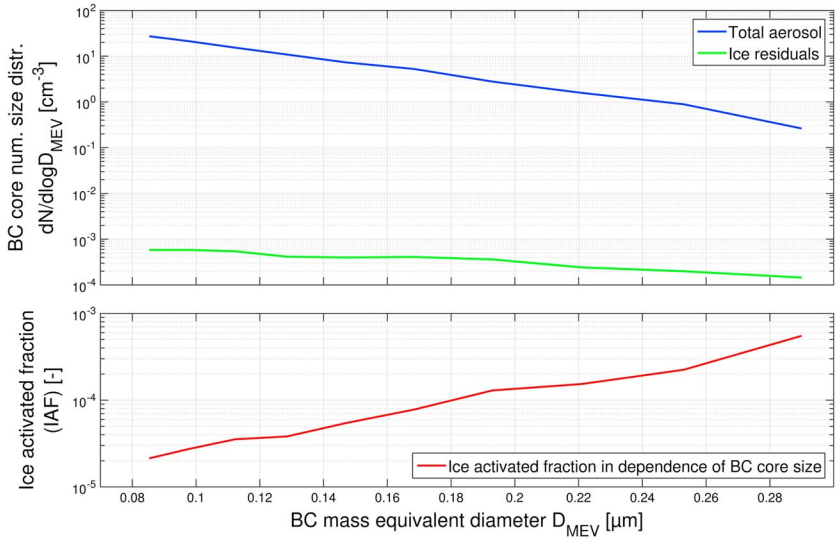

Figure 9. Size distributions of BC cores measured at TI and Ice-CVI and the ice activated fraction for BC-containing particles as a function of rBC mass equivalent diameter. D_{MEV} during CLACE 2013.

Based on the SP2 measurements, we conclude that the number of BC-containing particles in IR is very low. Furthermore, BC-containing particles are relatively depleted in the IR, with a number fraction of 1% in the IR population as compared to 12% in the total aerosol, based on SP2 measurements in the optical size range of 170 and 440 nm. Therefore, BC is not considered to play a significant role in nucleating ice at the Jungfraujoch. This result is in agreement with the study of *Kamphus et al.* [2010], who found no enrichment of BC in IR measured downstream of the Ice-CVI with an Aerosol Time-of-Flight Mass Spectrometer, and the study of *Chou et al.* [2011], who did not find any correlation between number concentrations of ice nucleating particles and BC mass (both studies were performed at the Jungfraujoch site). However, it is in contrast with the finding of *Cozic et al.* [2008], who found, in previous CLACE campaigns in 2004 and 2005, an enrichment of the BC mass fraction in submicrometer IR extracted using the Ice-CVI as compared to the submicrometer total aerosol, with BC mass fractions of 27% and 5%, respectively.

In order to understand the difference in the results obtained by *Cozic et al.* [2008] and those presented in this paper, it is necessary to consider the characteristics and limitations of the instruments used and the data processing procedure followed in the two respective studies. First of all, *Cozic et al.* [2008] determined BC mass fractions, whereas we report BC number fractions. BC mass fraction and BC number fraction are never perfectly correlated for variable aerosols. Indeed, the shift in the size distributions toward a higher fraction of larger particles in the IR compared to the total aerosol introduces a systematic bias in the direction of the observed discrepancy. However, while this may explain part of the discrepancy between the two studies, it certainly does not make a number-based depletion match with a mass-based enrichment. Possible measurement artifacts are more likely candidates. *Cozic et al.* [2008] applied a PSAP to quantify the equivalent black carbon (eBC) mass concentration. This is a filter-based technique, which provides a measure of the attenuation coefficient, from which the absorption coefficient is inferred as described by *Bond et al.* [1999]. The eBC mass concentration is finally inferred by assuming a mass absorption cross section (MAC) for the eBC (and assuming that all absorption is caused by BC). However, eBC mass concentrations inferred from absorption coefficients are tainted with considerable uncertainty due to the assumption to be made on the MAC, cross sensitivity to other absorbing components, such as mineral dust, as well as, to a lesser extent, to artifacts related to multiscattering enhancement within the filter matrix caused by aerosols with a high single scattering albedo.

The MAC value of the BC in the IR might be somewhat larger than the MAC values of the BC in the total aerosol due to differences in the lensing effect [e.g., *Schnaiter et al.*, 2005] if the BC in the IR has thicker coatings, as suggested by the results in section 3.4. However, this effect is too small to explain the observed discrepancy.

Cozic et al. [2008] attempted to correct the eBC mass determined for the IR for potential interference from mineral dust absorption. However, the dust interference may have been underestimated as detailed in section S8 of the supporting information [*Liu et al.*, 2010].

A further uncertainty in the interpretation of the results obtained by *Cozic et al.* [2008] is introduced by the fact that the BC mass fraction is calculated from the eBC mass measured for the whole sample divided by the aerosol mass inferred from the SMPS data for the submicrometer fraction only. The fact that the IR size distribution is shifted toward larger sizes compared to the total aerosol causes a larger truncation effect on aerosol mass for the ice residuals compared to the total aerosol, thereby introducing an artificial shift of the BC mass fraction toward larger values.

We cannot quantify which of the above effects play the dominant role in explaining the observed discrepancy. However, the above discussion highlights potential biases and pitfalls when using mass-based or absorption-based methods to assess the heterogeneous ice nucleation ability of BC. As it is the number of ice nucleating particles that is of importance, number-based methods should be favored when analyzing the importance of BC as heterogeneous INP. As such, we consider the SP2 to be a more robust measurement technique for this purpose.

3.4. Influence of BC Mixing State on Its IN Activity

The SP2 makes it possible to quantify the mixing state of BC with other particulate matter by combining the incandescence and light scattering signals. The coating thickness of BC cores with rBC mass equivalent diameters (D_{MEV}) in the range 170–220 nm was separately determined for the BC-containing particles in the total aerosol and the ice residuals, using the approach described in section 2.3.3. A comparison of the frequency of occurrence of the observed coating thickness values is shown in Figure 10 and reveals a distinct difference in the mixing state of the BC in the total aerosol and the ice residuals. The BC-containing particles in the total

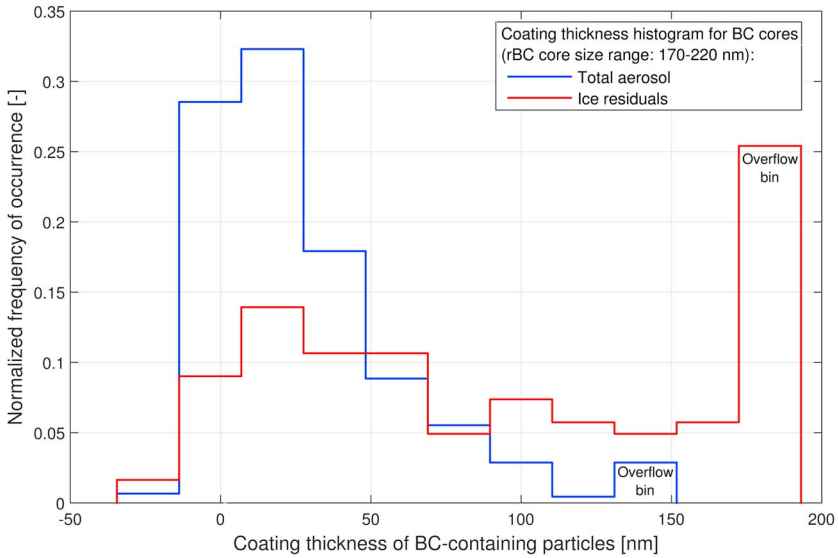

Figure 10. Coating thickness of BC-containing particles with an rBC mass equivalent core diameter in the range of 170 to 220 nm measured during simultaneous sampling downstream of the total inlet and the Ice-CVI using SP2. Note that the coating thickness range is restricted by different detection limits for the two SP2 instruments used; therefore, the "overflow bin", which shows the fraction of particles with coating thickness larger or equal the upper detection limit, appears at different positions.

aerosol were only moderately coated with a median value of 16 nm and a very minor fraction with coatings thicker than 100 nm. By contrast, the BC-containing particles in the ice residuals had much thicker coatings with a median value of 53 nm and a substantial fraction (45%) with coatings thicker than 100 nm.

Based on our findings, acquisition of coating by a BC core increases its ice nucleating ability. However, it is unclear whether this is due to an increase in the size of the particle (as described in the previous section, the likelihood of a particle acting as an INP increases with its size) or due to a change in its surface properties [*Chou et al.*, 2013]. Furthermore, it cannot be excluded that differences in observed coating are a result of preferential cloud processing of ice nucleating BC compared to BC that is not ice nucleating, where cloud processing refers to adsorption or absorption of semivolatile components or heterogeneous formation of secondary aerosol components from gas phase precursors absorbed into cloud droplets. However, this would probably only be the case if adsorption onto ice crystals is efficient and if (reactive) absorption into cloud droplets would either be negligible or reversed during the Wegener-Bergeron-Findeisen process occurring in the MPCs.

Previous studies of the influence of coating on ice nucleation by BC particles have resulted in a broad range of findings concerning the direction of the coating effect: *Möhler et al.* [2005] found that sulfuric acid decreased the ice nucleation activity of soot in the temperature range of −88°C to −43°C. On the contrary, *DeMott et al.* [1999] identified multilayer sulfuric acid coatings as enhancing ice nucleation as compared to uncoated soot at temperatures below −53°C and *Crawford et al.* [2011] found sulfuric acid coating of soot to reduce the ice activation threshold during cloud simulation experiments at the AIDA facility (temperature at the start of the expansion cooling experiments was typically −45°C). Meanwhile, organic coating and exposure to ozone, as in the case of uncoated soot, did not lead to heterogeneous ice nucleation above the experimental detection limit (set by the background counts which were in the range of 0.01–0.1% of the number of sampled particles) at −20°C and −30°C in a study by *Friedman et al.* [2011]. Similarly, *Chou et al.* [2013] did not identify photochemical aging of combustion aerosol in a smog chamber as having a noticeable effect on its ice nucleating ability at −30°C, −35°C, and −40°C, except for an experiment (at −35°C) during which a thicker organic coating was created, resulting in larger particles and an enhancement in their ice nucleating ability. Suppression of the ice nucleating abilitiy of coated black carbon is suggested by the findings of *Pratt et al.* [2010a]; aircraft measurements were conducted in a glaciated orographic wave cloud and while soot was enriched in cloud ice residuals compared to clear air aerosol, no aged soot (i.e., soot mixed with organic carbon and ammonium sulfate) was found in the ice residuals, even though such particles were present in clear air with a number fraction of 11 ± 1%.

If ice nucleation by BC-containing particles predominantly occurs via the immersion or condensation mode, the observed effect of coatings on the ice nucleating ability of BC-containing particles could be due to enhancement of the CCN activity of coated BC, leading to droplet activation and subsequent freezing. While freshly emitted BC does not show any significant CCN activity [*Liu et al.*, 2013, and references therein], coating of BC through condensation of secondary organic aerosols or sulphuric acid enhances its CCN activity [*Petzold et al.*, 2005; *Tritscher et al.*, 2011]. Considering our current understanding of the influence of coating on ice nucleation, it cannot be stated with certainty whether the increase in particle size, or the change in hydrophilicity, in the functional groups at the particle surface or in the shape of the particle was the dominating factor in increasing the ice nucleating ability of the sampled particles.

4. Conclusions

Particle size distributions, black carbon content, and coating thickness of BC-containing particles were measured for total aerosol and ice residuals in mixed-phase clouds at the Jungfraujoch. Larger particles were enriched in ice residuals, which corresponds to an increase in the ice activated fraction with particle size; IAFs were on the order of 10^{-4} to 10^{-3} for 100 nm (diameter) particles and 0.2 to 0.3 for 1 μm (diameter) particles. Nonetheless, size distributions show that submicrometer particles dominate the ice residual population by number (the number fraction of ice residuals in the 0.1 – 1 μm size range relative to the 0.1 – 5 μm size range is 0.89), due to their sheer number relative to supermicrometer particles in the total aerosol. Ice residual size distributions typically exhibited a maximum at 200 – 300 nm.

An empirical function for calculating the ice activated fraction was derived based on measurements conducted during CLACE 2013. The number concentration of INP estimated by means of this function is approximately 2 orders of magnitude higher than the INP number concentration predicted based on the parametrization put forward by *DeMott et al.* [2010] for the same aerosol and conditions, suggesting that the D2010 parametrization may provide estimates of INP which are substantially too low for the aerosols and cloud conditions probed at the Jungfraujoch during CLACE 2013.

As in the case of the overall ice residual population, the IAF of BC-containing particles increases with size, both with respect to total particle diameter and to BC core mass equivalent diameter. BC-containing particles were depleted in ice residuals, with an IAF for a given particle size approximately 1 order of magnitude lower than that of BC-free particles. The number-weighted mean IAF of BC-containing particles was below 10^{-4} for particles with BC cores smaller than ~300 nm (mass equivalent diameter). The number fraction-based finding that BC is depleted in ice residuals is in disagreement with a previous BC mass fraction-based study. While an analysis of the coating thickness of BC-containing particles provided evidence that acquisition of coatings by BC cores increases the ice nucleating activity of BC in mixed-phase clouds, BC-containing particles were found not to play an important role in nucleating ice at the Jungfraujoch, and BC-free particles are of much greater relevance for the INP number. Extrapolating the finding that BC is depleted in ice residuals on a global scale would provide strong evidence that a potential anthropogenic climate impact of BC via the glaciation effect in mixed-phase clouds [*Lohmann*, 2002] is likely to be negligible. Results regarding the role of black carbon as an INP, and the influence of its mixing state on its ice nucleating ability, remain contradictory. Further field studies of ambient ice residuals, especially using single particle instruments, as well as laboratory studies on the effect of BC coatings on its ice nucleating properties are needed to understand the importance of BC under different meteorological conditions and to understand the role of the nucleation scavenging pathway through the ice phase for the life cycle of atmospheric BC particles.

Acknowledgments
This project is funded by the Swiss National Science Foundation (grant 135356), the DFG priority program HALO (SPP1294, grant ME3534/1-2), the DFG research unit INUIT (grants FOR1525, STR453/7-1, and SCHN1138/2-1), the DFG (grant SCHN1140/2-1), MeteoSwiss (GAW-CH program), the European Research Council (grant 615922-BLACARAT), the ACTRIS program (European Union Seventh Framework Program (FP7/2007-2013), grant 262254) and the BACCHUS project (European Union Seventh Framework Program (FP7/2007-2013), grant 603445). We thank the International Foundation High Altitude Research Stations Jungfraujoch and Gornergrat (HFSJG) for the opportunity to perform experiments on the Jungfraujoch. We also thank MeteoSwiss for providing the meteorological data, E. Hammer for processing the ice residual SMPS data, E. Herrmann for providing the GAW data, N. Bukowiecki for maintaining the Jungfraujoch data chain and infrastructure, I. Crawford for providing the WIBS3 data, S. Schmidt and T. Klimach for OPSS operation and data acquisition, and C. Linke and R. Färber for their assistance in Single Particle Soot Photometer setup and operation, respectively. The aerosol data are archived at the Paul Scherrer Institute and are available upon request (email: martin.gysel@psi.ch). The meteorological data are available from MeteoSwiss.

References

Archuleta, C. M., P. J. DeMott, and S. M. Kreidenweis (2005), Ice nucleation by surrogates for atmospheric mineral dust and mineral dust/sulfate particles at cirrus temperatures, *Atmos. Chem. Phys.*, *5*(10), 2617 – 2634, doi:10.5194/acp-5-2617-2005.

Baltensperger, U., M. Schwikowski, D. Jost, S. Nyeki, H. Gäggeler, and O. Poulida (1998), Scavenging of atmospheric constituents in mixed phase clouds at the high-alpine site Jungfraujoch Part I: Basic concept and aerosol scavenging by clouds, *Atmos. Environ.*, *32*(23), 3975 – 3983, doi:10.1016/S1352-2310(98)00051-X.

Baumgardner, D., et al. (2012), Soot reference materials for instrument calibration and intercomparisons: A workshop summary with recommendations, *Atmos. Meas. Tech.*, *5*(8), 1869 – 1887, doi:10.5194/amt-5-1869-2012.

Bond, T. C., T. L. Anderson, and D. Campbell (1999), Calibration and intercomparison of filter-based measurements of visible light absorption by aerosols, *Aerosol Sci. Technol.*, *30*(6), 582 – 600, doi:10.1080/027868299304435.

Boose, Y., et al. (2016), Ice nucleating particle measurements at 241 K during winter months at 3580 m msl in the Swiss Alps, *J. Atmos. Sci.*, *73*(5), 2203 – 2228, doi:10.1175/JAS-D-15-0236.1.

Bukowiecki, N., E. Weingartner, M. Gysel, M. Collaud Coen, P. Zieger, E. Herrmann, M. Steinbacher, H. W. Gäggeler, and U. Baltensperger (2016), A review of more than 20 years of aerosol observation at the High Altitude Research Station Jungfraujoch, Switzerland (3580 m asl), *Aerosol Air Qual. Res.*, *16*(3), 764–788, doi:10.4209/aaqr.2015.05.0305.

Burkart, J., G. Steiner, G. Reischl, H. Moshammer, M. Neuberger, and R. Hitzenberger (2010), Characterizing the performance of two optical particle counters (Grimm OPC1.108 and OPC1.109) under urban aerosol conditions, *J. Aerosol Sci.*, *41*(10), 953–962, doi:10.1016/j.jaerosci.2010.07.007.

Cai, Y., D. C. Montague, W. Mooiweer-Bryan, and T. Deshler (2008), Performance characteristics of the ultra high sensitivity aerosol spectrometer for particles between 55 and 800 nm: Laboratory and field studies, *J. Aerosol Sci.*, *39*(9), 759–769, doi:10.1016/j.jaerosci.2008.04.007.

Chen, J.-P., and D. Lamb (1999), Simulation of cloud microphysical and chemical processes using a multicomponent framework. Part II: Microphysical evolution of a wintertime orographic cloud, *J. Atmos. Sci.*, *56*(14), 2293–2312, doi:10.1175/1520-0469(1999)056<2293:SOCMAC>2.0.CO;2.

Chou, C., O. Stetzer, E. Weingartner, Z. Jurányi, Z. A. Kanji, and U. Lohmann (2011), Ice nuclei properties within a Saharan dust event at the Jungfraujoch in the Swiss Alps, *Atmos. Chem. Phys.*, *11*(10), 4725–4738, doi:10.5194/acp-11-4725-2011.

Chou, C., Z. A. Kanji, O. Stetzer, T. Tritscher, R. Chirico, M. F. Heringa, E. Weingartner, A. S. H. Prévôt, U. Baltensperger, and U. Lohmann (2013), Effect of photochemical ageing on the ice nucleation properties of diesel and wood burning particles, *Atmos. Chem. Phys.*, *13*(2), 761–772, doi:10.5194/acp-13-761-2013.

Connolly, P. J., O. Möhler, P. R. Field, H. Saathoff, R. Burgess, T. Choularton, and M. Gallagher (2009), Studies of heterogeneous freezing by three different desert dust samples, *Atmos. Chem. Phys.*, *9*(8), 2805–2824, doi:10.5194/acp-9-2805-2009.

Cozic, J., S. Mertes, B. Verheggen, D. J. Cziczo, S. J. Gallavardin, S. Walter, U. Baltensperger, and E. Weingartner (2008), Black carbon enrichment in atmospheric ice particle residuals observed in lower tropospheric mixed phase clouds, *J. Geophys. Res.*, *113*, D15209, doi:10.1029/2007JD009266.

Crawford, I., et al. (2011), Studies of propane flame soot acting as heterogeneous ice nuclei in conjunction with single particle soot photometer measurements, *Atmos. Chem. Phys.*, *11*(18), 9549–9561, doi:10.5194/acp-11-9549-2011.

Cziczo, D. J., et al. (2009), Inadvertent climate modification due to anthropogenic lead, *Nat. Geosci.*, *2*(5), 333–336, doi:10.1038/ngeo499.

Cziczo, D. J., K. D. Froyd, C. Hoose, E. J. Jensen, M. Diao, M. A. Zondlo, J. B. Smith, C. H. Twohy, and D. M. Murphy (2013), Clarifying the dominant sources and mechanisms of cirrus cloud formation, *Science*, *340*(6138), 1320–1324, doi:10.1126/science.1234145.

Dahlkötter, F., M. Gysel, D. Sauer, A. Minikin, R. Baumann, P. Seifert, A. Ansmann, M. Fromm, C. Voigt, and B. Weinzierl (2014), The Pagami Creek smoke plume after long-range transport to the upper troposphere over Europe—Aerosol properties and black carbon mixing state, *Atmos. Chem. Phys.*, *14*(12), 6111–6137, doi:10.5194/acp-14-6111-2014.

DeMott, P. J., Y. Chen, S. M. Kreidenweis, D. C. Rogers, and D. E. Sherman (1999), Ice formation by black carbon particles, *Geophys. Res. Lett.*, *26*(16), 2429–2432, doi:10.1029/1999GL900580.

DeMott, P. J., A. J. Prenni, X. Liu, S. M. Kreidenweis, M. D. Petters, C. H. Twohy, M. S. Richardson, T. Eidhammer, and D. C. Rogers (2010), Predicting global atmospheric ice nuclei distributions and their impacts on climate, *Proc. Natl. Acad. Sci.*, *107*(25), 11,217–11,222, doi:10.1073/pnas.0910818107.

Ebert, M., A. Worringen, N. Benker, S. Mertes, E. Weingartner, and S. Weinbruch (2011), Chemical composition and mixing-state of ice residuals sampled within mixed phase clouds, *Atmos. Chem. Phys.*, *11*(6), 2805–2816, doi:10.5194/acp-11-2805-2011.

Foot, V. E., P. H. Kaye, W. R. Stanley, S. J. Barrington, M. Gallagher, and A. Gabey (2008), Low-cost real-time multiparameter bio-aerosol sensors, *Proc. SPIE*, *7116*, 1–12, doi:10.1117/12.800226.

Friedman, B., G. Kulkarni, J. Beránek, A. Zelenyuk, J. A. Thornton, and D. J. Cziczo (2011), Ice nucleation and droplet formation by bare and coated soot particles, *J. Geophys. Res.*, *116*, D17203, doi:10.1029/2011JD015999.

Gabey, A. M., M. W. Gallagher, J. Whitehead, J. R. Dorsey, P. H. Kaye, and W. R. Stanley (2010), Measurements and comparison of primary biological aerosol above and below a tropical forest canopy using a dual channel fluorescence spectrometer, *Atmos. Chem. Phys.*, *10*(10), 4453–4466, doi:10.5194/acp-10-4453-2010.

Gabey, A. M., W. R. Stanley, M. W. Gallagher, and P. H. Kaye (2011), The fluorescence properties of aerosol larger than 0.8 μm in urban and tropical rainforest locations, *Atmos. Chem. Phys.*, *11*(11), 5491–5504, doi:10.5194/acp-11-5491-2011.

Gao, R. S., et al. (2007), A novel method for estimating light-scattering properties of soot aerosols using a modified single-particle soot photometer, *Aerosol Sci. Technol.*, *41*(2), 125–135, doi:10.1080/02786820601118398.

Gerber, H. (1991), Direct measurement of suspended particulate volume concentration and far-infrared extinction coefficient with a laser-diffraction instrument, *Appl. Opt.*, *30*(33), 4824–4831, doi:10.1364/AO.30.004824.

Gysel, M., M. Laborde, J. S. Olfert, R. Subramanian, and A. J. Gröhn (2011), Effective density of Aquadag and fullerene soot black carbon reference materials used for SP2 calibration, *Atmos. Meas. Tech.*, *4*(12), 2851–2858, doi:10.5194/amt-4-2851-2011.

Hallett, J., and S. C. Mossop (1974), Production of secondary ice particles during the riming process, *Nature*, *249*(5452), 26–28, doi:10.1038/249026a0.

Herrmann, E., et al. (2015), Analysis of long-term aerosol size distribution data from Jungfraujoch with emphasis on free tropospheric conditions, cloud influence, and air mass transport, *J. Geophys. Res. Atmos.*, *120*(18), 9459–9480, doi:10.1002/2015JD023660.

Hiranuma, N., S. D. Brooks, R. C. Moffet, A. Glen, A. Laskin, M. K. Gilles, P. Liu, A. M. Macdonald, J. W. Strapp, and G. M. McFarquhar (2013), Chemical characterization of individual particles and residuals of cloud droplets and ice crystals collected on board research aircraft in the ISDAC 2008 study, *J. Geophys. Res. Atmos.*, *118*(12), 6564–6579, doi:10.1002/jgrd.50484.

Hoose, C., and O. Möhler (2012), Heterogeneous ice nucleation on atmospheric aerosols: A review of results from laboratory experiments, *Atmos. Chem. Phys.*, *12*(20), 9817–9854, doi:10.5194/acp-12-9817-2012.

Hung, H.-M., A. Malinowski, and S. T. Martin (2003), Kinetics of heterogeneous ice nucleation on the surfaces of mineral dust cores inserted into aqueous ammonium sulfate particles, *J. Phys. Chem. A*, *107*(9), 1296–1306, doi:10.1021/jp021593y.

Järvinen, E., et al. (2016), Quasi-spherical ice in convective clouds, *J. Atmos. Sci.*, *73*, 3885–3910, doi:10.1175/JAS-D-15-0365.1.

Kamphus, M., M. Ettner-Mahl, T. Klimach, F. Drewnick, L. Keller, D. J. Cziczo, S. Mertes, S. Borrmann, and J. Curtius (2010), Chemical composition of ambient aerosol, ice residues and cloud droplet residues in mixed-phase clouds: Single particle analysis during the Cloud and Aerosol Characterization Experiment (CLACE 6), *Atmos. Chem. Phys.*, *10*(16), 8077–8095, doi:10.5194/acp-10-8077-2010.

Kaye, P., W. R. Stanley, E. Hirst, E. V. Foot, K. L. Baxter, and S. J. Barrington (2005), Single particle multichannel bio-aerosol fluorescence sensor, *Opt. Express*, *13*(10), 3583–3593, doi:10.1364/OPEX.13.003583.

Kaye, P. H., E. Hirst, R. S. Greenaway, Z. Ulanowski, E. Hesse, P. J. DeMott, C. Saunders, and P. Connolly (2008), Classifying atmospheric ice crystals by spatial light scattering, *Opt. Lett.*, *33*(13), 1545–1547, doi:10.1364/OL.33.001545.

Korolev, A. (2007), Limitations of the Wegener–Bergeron–Findeisen mechanism in the evolution of mixed–phase clouds, *J. Atmos. Sci.*, *64*(9), 3372–3375, doi:10.1175/JAS4035.1.

Kupiszewski, P., E. Weingartner, P. Vochezer, M. Schnaiter, A. Bigi, M. Gysel, B. Rosati, E. Toprak, S. Mertes, and U. Baltensperger (2015), The ice selective inlet: A novel technique for exclusive extraction of pristine ice crystals in mixed-phase clouds, *Atmos. Meas. Tech.*, *8*(8), 3087–3106, doi:10.5194/amt-8-3087-2015.

Laborde, M., et al. (2012a), Single particle soot photometer intercomparison at the AIDA chamber, *Atmos. Meas. Tech.*, *5*(12), 3077–3097, doi:10.5194/amt-5-3077-2012.

Laborde, M., P. Mertes, P. Zieger, J. Dommen, U. Baltensperger, and M. Gysel (2012b), Sensitivity of the single particle soot photometer to different black carbon types, *Atmos. Meas. Tech.*, *5*(5), 1031–1043, doi:10.5194/amt-5-1031-2012.

Laborde, M., et al. (2013), Black carbon physical properties and mixing state in the European megacity Paris, *Atmos. Chem. Phys.*, *13*(11), 5831–5856, doi:10.5194/acp-13-5831-2013.

Lamb, D., and J. Verlinde (2011), *Physics and Chemistry of Clouds*, Cambridge Univ. Press, New York.

Lance, S., C. A. Brock, D. Rogers, and J. A. Gordon (2010), Water droplet calibration of the Cloud Droplet Probe (CDP) and in-flight performance in liquid, ice and mixed-phase clouds during ARCPAC, *Atmos. Meas. Tech.*, *3*(6), 1683–1706, doi:10.5194/amt-3-1683-2010.

Lawson, R. P., S. Woods, and H. Morrison (2015), The microphysics of ice and precipitation development in tropical cumulus clouds, *J. Atmos. Sci.*, *72*(6), 2429–2445, doi:10.1175/JAS-D-14-0274.1.

Liu, D., et al. (2010), Single particle characterization of black carbon aerosols at a tropospheric alpine site in Switzerland, *Atmos. Chem. Phys.*, *10*(15), 7389–7407, doi:10.5194/acp-10-7389-2010.

Liu, D., J. Allan, J. Whitehead, D. Young, M. Flynn, H. Coe, G. McFiggans, Z. L. Fleming, and B. Bandy (2013), Ambient black carbon particle hygroscopic properties controlled by mixing state and composition, *Atmos. Chem. Phys.*, *13*(4), 2015–2029, doi:10.5194/acp-13-2015-2013.

Lloyd, G., et al. (2015), The origins of ice crystals measured in mixed-phase clouds at the high-alpine site Jungfraujoch, *Atmos. Chem. Phys.*, *15*(22), 12,953–12,969, doi:10.5194/acp-15-12953-2015.

Lohmann, U. (2002), A glaciation indirect aerosol effect caused by soot aerosols, *Geophys. Res. Lett.*, *29*(4), 1052, doi:10.1029/2001GL014357.

Lohmann, U., and J. Feichter (2005), Global indirect aerosol effects: A review, *Atmos. Chem. Phys.*, *5*(3), 715–737, doi:10.5194/acp-5-715-2005.

Marcolli, C., S. Gedamke, T. Peter, and B. Zobrist (2007), Efficiency of immersion mode ice nucleation on surrogates of mineral dust, *Atmos. Chem. Phys.*, *7*(19), 5081–5091, doi:10.5194/acp-7-5081-2007.

Mertes, S., et al. (2007), Counterflow virtual impactor based collection of small ice particles in mixed-phase clouds for the physico-chemical characterization of tropospheric ice nuclei: Sampler description and first case study, *Aerosol Sci. Technol.*, *41*(9), 848–864, doi:10.1080/02786820701501881.

Möhler, O., et al. (2005), Effect of sulfuric acid coating on heterogeneous ice nucleation by soot aerosol particles, *J. Geophys. Res.*, *110*, D11210, doi:10.1029/2004JD005169.

Moteki, N., and Y. Kondo (2007), Effects of mixing state on black carbon measurements by laser-induced incandescence, *Aerosol Sci. Technol.*, *41*(4), 398–417, doi:10.1080/02786820701199728.

Moteki, N., Y. Kondo, and S. Nakamura (2010), Method to measure refractive indices of small nonspherical particles: Application to black carbon particles, *J. Aerosol Sci.*, *41*(5), 513–521, doi:10.1016/j.jaerosci.2010.02.013.

Moteki, N., Y. Kondo, N. Oshima, N. Takegawa, M. Koike, K. Kita, H. Matsui, and M. Kajino (2012), Size dependence of wet removal of black carbon aerosols during transport from the boundary layer to the free troposphere, *Geophys. Res. Lett.*, *39*, doi:10.1029/2012GL052034.

Murray, B. J., D. O'Sullivan, J. D. Atkinson, and M. E. Webb (2012), Ice nucleation by particles immersed in supercooled cloud droplets, *Chem. Soc. Rev.*, *41*, 6519–6554, doi:10.1039/C2CS35200A.

Niedermeier, D., R. A. Shaw, S. Hartmann, H. Wex, T. Clauss, J. Voigtländer, and F. Stratmann (2011), Heterogeneous ice nucleation: Exploring the transition from stochastic to singular freezing behavior, *Atmos. Chem. Phys.*, *11*(16), 8767–8775, doi:10.5194/acp-11-8767-2011.

Petzold, A., M. Gysel, X. Vancassel, R. Hitzenberger, H. Puxbaum, S. Vrochticky, E. Weingartner, U. Baltensperger, and P. Mirabel (2005), On the effects of organic matter and sulphur-containing compounds on the ccn activation of combustion particles, *Atmos. Chem. Phys.*, *5*(12), 3187–3203, doi:10.5194/acp-5-3187-2005.

Phillips, V. T. J., A. M. Blyth, P. R. A. Brown, T. W. Choularton, and J. Latham (2001), The glaciation of a cumulus cloud over New Mexico, *Q. J. R. Meteorolog. Soc.*, *127*(575), 1513–1534, doi:10.1002/qj.49712757503.

Pratt, K. A., P. J. DeMott, J. R. French, Z. Wang, D. L. Westphal, A. J. Heymsfield, C. H. Twohy, A. J. Prenni, and K. A. Prather (2009), In situ detection of biological particles in cloud ice-crystals, *Nat. Geosci.*, *2*(6), 398–401, doi:10.1038/ngeo521.

Pratt, K. A., A. J. Heymsfield, C. H. Twohy, S. M. Murphy, P. J. DeMott, J. G. Hudson, R. Subramanian, Z. Wang, J. H. Seinfeld, and K. A. Prather (2010a), In situ chemical characterization of aged biomass-burning aerosols impacting cold wave clouds, *J. Atmos. Sci.*, *67*(8), 2451–2468, doi:10.1175/2010JAS3330.1.

Pratt, K. A., et al. (2010b), Observation of playa salts as nuclei in orographic wave clouds, *J. Geophys. Res.*, *115*, D15301, doi:10.1029/2009JD013606.

Prenni, A. J., P. J. DeMott, C. Twohy, M. R. Poellot, S. M. Kreidenweis, D. C. Rogers, S. D. Brooks, M. S. Richardson, and A. J. Heymsfield (2007), Examinations of ice formation processes in Florida cumuli using ice nuclei measurements of anvil ice crystal particle residues, *J. Geophys. Res.*, *112*, D10221, doi:10.1029/2006JD007549.

Pruppacher, H. R., and J. D. Klett (1997), *Microphysics of Clouds and Precipitation*, 2nd edn., Kluwer Acad. Publ., Dordrecht, The Netherlands.

Saunders, C., and A. Hosseini (2001), A laboratory study of the effect of velocity on Hallett-Mossop ice crystal multiplication, *Atmos. Res.*, *59–60*, 3–14, doi:10.1016/S0169-8095(01)00106-5.

Schnaiter, M., C. Linke, O. Möhler, K.-H. Naumann, H. Saathoff, R. Wagner, U. Schurath, and B. Wehner (2005), Absorption amplification of black carbon internally mixed with secondary organic aerosol, *J. Geophys. Res.*, *110*, D19204, doi:10.1029/2005JD006046.

Schnaiter, M., et al. (2016), Cloud chamber experiments on the origin of ice crystal complexity in cirrus clouds, *Atmos. Chem. Phys.*, *16*(8), 5091–5110, doi:10.5194/acp-16-5091-2016.

Schwarz, J. P., et al. (2006), Single-particle measurements of midlatitude black carbon and light-scattering aerosols from the boundary layer to the lower stratosphere, *J. Geophys. Res.*, *111*, D16207, doi:10.1029/2006JD007076.

Schwarz, J. P., et al. (2008), Measurement of the mixing state, mass, and optical size of individual black carbon particles in urban and biomass burning emissions, *Geophys. Res. Lett.*, *35*, L13810, doi:10.1029/2008GL033968.

Schwarzenböck, A., S. Mertes, W. Heintzenberg, J. Wobrock, and P. Laj (2001), Impact of the Bergeron-Findeisen process on the release of aerosol particles during the evolution of cloud ice, *Atmos. Res.*, *58*(4), 295–313, doi:10.1016/S0169-8095(01)00096-5.

Schwarzenboeck, A., J. Heintzenberg, and S. Mertes (2000), Incorporation of aerosol particles between 25 and 850 nm into cloud elements: Measurements with a new complementary sampling system, *Atmos. Res.*, *52*(4), 241–260, doi:10.1016/S0169-8095(99)00034-4.

Seinfeld, J. H., and S. N. Pandis (2006), *Atmospheric Chemistry and Physics: From Air Pollution to Climate Change*, 2nd ed., John Wiley Inc., Hoboken, N. J.

Stephens, M., N. Turner, and J. Sandberg (2003), Particle identification by laser-induced incandescence in a solid-state laser cavity, *Appl. Opt.*, *42*(19), 3726–3736, doi:10.1364/AO.42.003726.

Stopelli, E., F. Conen, C. E. Morris, E. Herrmann, N. Bukowiecki, and C. Alewell (2015), Ice nucleation active particles are efficiently removed by precipitating clouds, *Sci. Rep.*, *5*, 16433, doi:10.1038/srep16433.

Sun, Z., and K. P. Shine (1994), Studies of the radiative properties of ice and mixed-phase clouds, *Q. J. R. Meteorolog. Soc.*, *120*(515), 111–137, doi:10.1002/qj.49712051508.

Szyrmer, W., and I. Zawadzki (1997), Biogenic and anthropogenic sources of ice-forming nuclei: A review, *Bull. Amer. Meteor. Soc.*, *78*, 209–209, doi:10.1175/1520-0477(1997)078<0209:BAASOI>2.0.CO;2.

Tritscher, T., Z. Jurányi, M. Martin, R. Chirico, M. Gysel, M. F. Heringa, P. F. DeCarlo, B. Sierau, A. S. H. Prévôt, E. Weingartner, and U. Baltensperger (2011), Changes of hygroscopicity and morphology during ageing of diesel soot, *Environ. Res. Lett.*, *6*(3), 034026, doi:10.1088/1748-9326/6/3/034026.

Twohy, C. H., and M. R. Poellot (2005), Chemical characteristics of ice residual nuclei in anvil cirrus clouds: Evidence for homogeneous and heterogeneous ice formation, *Atmos. Chem. Phys.*, *5*(8), 2289–2297, doi:10.5194/acp-5-2289-2005.

Ulanowski, Z., P. H. Kaye, E. Hirst, R. S. Greenaway, R. J. Cotton, E. Hesse, and C. T. Collier (2014), Incidence of rough and irregular atmospheric ice particles from small ice detector 3 measurements, *Atmos. Chem. Phys.*, *14*(3), 1649–1662, doi:10.5194/acp-14-1649-2014.

Vali, G., P. J. DeMott, O. Möhler, and T. F. Whale (2015), Technical note: A proposal for ice nucleation terminology, *Atmos. Chem. Phys.*, *15*(18), 10,263–10,270, doi:10.5194/acp-15-10263-2015.

Verheggen, B., J. Cozic, E. Weingartner, K. Bower, S. Mertes, P. Connolly, M. Gallagher, M. Flynn, T. Choularton, and U. Baltensperger (2007), Aerosol partitioning between the interstitial and the condensed phase in mixed-phase clouds, *J. Geophys. Res.*, *112*, D23202, doi:10.1029/2007JD008714.

Vochezer, P., E. Järvinen, R. Wagner, P. Kupiszewski, T. Leisner, and M. Schnaiter (2016), In situ characterization of mixed phase clouds using the small ice detector and the particle phase discriminator, *Atmos. Meas. Tech.*, *9*(1), 159–177, doi:10.5194/amt-9-159-2016.

von der Weiden, S.-L., F. Drewnick, and S. Borrmann (2009), Particle loss calculator—A new software tool for the assessment of the performance of aerosol inlet systems, *Atmos. Meas. Tech.*, *2*(2), 479–494, doi:10.5194/amt-2-479-2009.

Weingartner, E., S. Nyeki, and U. Baltensperger (1999), Seasonal and diurnal variation of aerosol size distributions ($10 < d < 750$ nm) at a high-alpine site (Jungfraujoch 3580 m asl), *J. Geophys. Res.*, *104*(D21), 26,809–26,820, doi:10.1029/1999JD900170.

Wendisch, M., T. J. Garrett, and J. W. Strapp (2002), Wind tunnel tests of the airborne PVM-100A response to large droplets, *J. Atmos. Oceanic Tech.*, *19*(10), 1577–1584, doi:10.1175/1520-0426(2002)019<1577:WTTOTA>2.0.CO;2.

Wiedensohler, A., et al. (2012), Mobility particle size spectrometers: Harmonization of technical standards and data structure to facilitate high quality long-term observations of atmospheric particle number size distributions, *Atmos. Meas. Tech.*, *5*(3), 657–685, doi:10.5194/amt-5-657-2012.

Worringen, A., et al. (2015), Single-particle characterization of ice-nucleating particles and ice particle residuals sampled by three different techniques, *Atmos. Chem. Phys.*, *15*(8), 4161–4178, doi:10.5194/acp-15-4161-2015.

Yano, J. I., and V. T. J. Phillips (2011), Ice-ice collisions: An ice multiplication process in atmospheric clouds, *J. Atmos. Sci.*, *68*(2), 322–333, doi:10.1175/2010JAS3607.1.